DOE/ER/10566--T2

DOE/ER/10566--T2

DE83 017509

Technical Progress Report

for the Department of Energy

Contract No. DE-AC02-80-ER10566.A005

UMass Referral No. 5-28875

Principal Investigator: Mireille T. Clapp

Department of Mechanical Engineering

University of Massachusetts

Amherst, MA 01003

Phone: (413) 545-0868

Main Office: (413) 545-2505

DISCLAIMER

TABLE OF CONTENTS

DOE/ER/10566--T9

ION IMPLANTATION AND SPIN QUENCHING OF SUPERCONDUCTING MATERIALS

I. INTRODUCTION

A great deal of interest has been focused on the A-15 structure because of its advantageous superconducting properties. Progress in this field seems to involve highly metastable A-15 compounds. An inherent problem with A-15 materials is that they are brittle, presenting complications with the manufacture of wires. However there are new processing techniques that suggest possible solutions. Ion implantation is a way of accurately modifying surface composition and of forming metastable phases. Spin quenching (melt spinning) is a very rapid solidification technique capable of producing metastable A-15's as well as amorphous and extremely ductile tapes which can subsequently be annealed into the A-15 structure. This year's work has focused on completing the experiments on heavy dose implantations into A-15 substrates and on initiating experiments on melt spinning for forming new A-15 compounds and amorphous ribbons.

II. THE EFFECT OF HEAVY DOSE IMPLANTATIONS OF B AND C ON THE CRYSTAL STRUCTURE AND SUPERCONDUCTING TRANSITION TEMPERATURE OF A-15 Nb_3Al.

The effect of ion implantation on metastable phase formation and superconducting transition temperature (T_c) has been investigated. The particular alloys studied were $Nb_3Al_{1-x}B_x$ and $Nb_3Al_{1-x}C_x$. A-15 Nb_3Al was used as the substrate material. Large doses of B and C (up to 23 At%) were implanted into Al depleted surfaces. A series of implantation energies and

doses was chosen to maintain the (Al + B) and (Al + C) concentrations equal to 25 At%. This is necessary for achieving high T_c materials. Auger analysis indicated that there was very good agreement between experimental and theoretical dopant profiles immediately after implantation. After annealing up to 900°C the B atoms showed very little redistribution; however the C atoms tended to migrate towards the surface. Structural analysis using a READ camera and a diffractometer indicated that the large doses of B and C had been implanted into the A-15 structure without affecting its stability; this A-15 phase remained stable up to 950°C. Implantation caused the lattice parameter of the A-15 phase to increase by 1 to 2%. There was no increase in the superconducting transition temperature above that of the substrate (18 K). The defects associated with heavy dose implantation appear to be detrimental for forming high T_c materials; they cause an increase in lattice parameter and for a given alloy system T_c decreases as a_o increases. For this reason future work will be confined to low dose implantation where radiation damage is far less severe.

Details of this investigation have been given in previous progress reports. The work was completed earlier this year and is now being published in the Journal of Applied Physics. A preprint of the paper is included at the end of this report. (Appendix A)

III. MELT SPINNING AND THE SEARCH FOR NEW AMORPHOUS METALS AND A-15 COMPOUNDS

A. Optimization of Melt Spinning Apparatus.

A schematic of the chill block melt spinning apparatus used in this research is shown in Figure 1. Master alloys were melted with a 2.5 kW induction heater under an argon pressure of about 500 torr. When the alloys became visibly molten, the induction current was shut off and, simultaneously, argon pressure was applied above the melt. As a result, a molten jet was ejected from the crucible nozzle onto the outer surface of the copper substrate wheel (178 mm diameter) which was rotating at several thousand rpm. The ejected melt was rapidly quenched on the wheel surface in the form of thin ribbons. For all melt spinning experiments, the melt jet was incident at an angle of 15^{o} to the perpendicular to the wheel surface.

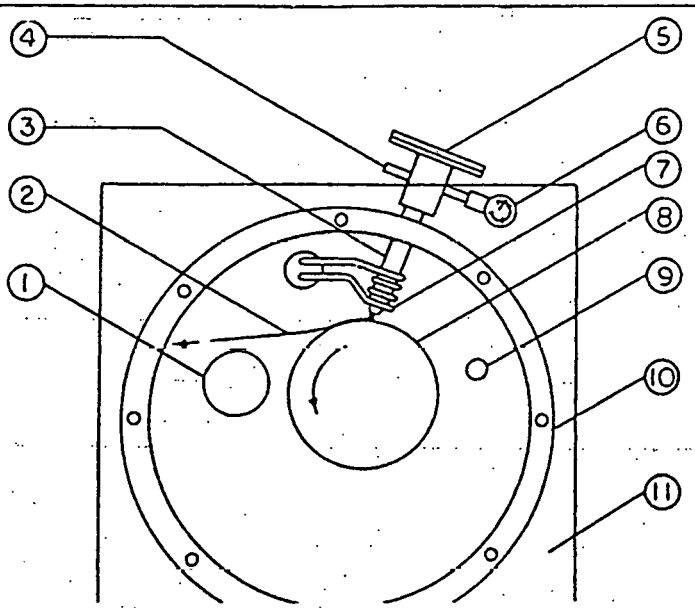

(1) Evacuation port; (2) Cast ribbon; (3) Crucible; (4) Argon gas inlet; (5) Viewport; (6) Vacuum gauge; (7) Induction coil; (8) Copper substrate wheel; (9) Argon gas inlet; (10) Steel chamber; (11) Lexan cover plate.

FIG. 1. Schematic of chill block melt spinning machine - front view.

The performance of the machine was assessed by studying the effects of two process parameters--substrate surface speed and melt jet ejection pressure--on the geometry and quality of $Fe_{40}Ni_{40}B_{20}$ and $Cu_{76}Al_{14}Ni_{10}$ ribbons. The effects of these parameters were in general agreement with those cited in the literature. Increasing the substrate surface speed decreased the ribbon thickness (increased the quench rate), but had no well-defined effect on the ribbon width. Increasing the melt jet ejection pressure increased the ribbon thickness (decreased the quench rate) and increased the ribbon width. In addition, an amorphous phase was observed in cast $Fe_{40}Ni_{40}B_{20}$ ribbons.

The alloys studied in this research had very high melting temperatures causing problems with crucible melting (e.g. quartz) or crucible contamination (e.g. alumina). This problem was solved by suspending the sample in such a way that it did not touch the crucible. This eliminated heat conduction from the sample to the crucible. This also prevented any contamination to the sample from the crucible. The instant the sample melted, the ejection pressure was applied. This allowed the sample to be quenched as soon as it became molten, preventing heating of the sample above the melting point and thus improving cooling rates. A description of one of our suspension apparati can be seen in Appendix B.

B. New Amorphous Metals and A-15 Compounds

1. Quaternaries

The melt spinning apparatus was initially tested with the $V_2CrAl_{1-x}B_x$ and $Ti_3Nb_6Mo_3Si_4$ quaternary systems. These alloys were chosen for several reasons. Most superconductivity research has concentrated on binaries and ternaries; much less has been done on quaternaries. The particular combination of atoms agreed well with Hartsough's rules for A-15 phase stability. The transition elements have a high probability of forming the A-15 phase. The atomic radius ratio of the transition elements to the non-transition elements is favorable. The electron to atom ratio is 4.75 which is optimum for A-15 phase formation as well as high T_c superconductors.

Initial work on these alloys showed that melt spinning had no significant effect on the crystal structure of the $V_2CrAl_{1-x}B_x$ alloys but a large effect on the $Ti_3Nb_6Mo_3Si_4$ alloys. The equilibrium phases of these latter alloys are the high temperature Nb_5Si_3 type and the bcc NbTiMo solid solution. Melt spinning had the effect of promoting the formation of a third phase , a <u>new</u> $(NbTiMo)_3Si$ A-15 phase. The lattice parameter of the A-15 phase was 5.08Å, intermediary between values of 5.12 Å for Nb_3Si and 4.89Å for Mo_3Si. Melt spinning increased the superconducting transition temperature of the $Ti_3Nb_6Mo_3Si_4$ alloys from 1.9 to 3.4K.

The more rapid the quenching rate, the more A-15 phase was produced. This indicated that very interesting results could be obtained by further increasing the cooling rates of our melt spinning apparatus. Another interesting observation that was made on these alloys was that melt spinning increased the Vickers microhardness values of the $V_2CrAl_{1-x}B_x$

alloys from 500 to 750, and of the $Ti_3Nb_6Mo_3Si_4$ alloys from 1000 to as high as 1675.

Details of this work are being published in the Proceedings of the International Conference on Phase Transformations in Solids. A preprint can be found in Appendix B.

Work has continued on the $Ti_3Nb_6Mo_3Si_4$ system. By significantly increasing the quenching rates, single phase A-15 and amorphous ribbons have been obtained. This was achieved by modifying the processing parameters in the following fashion: increasing the wheel speed from 37 to 53 m/sec; decreasing the orifice diameter to 0.8 mm; decreasing the gap between the crucible and the wheel to 1.5 mm; decreasing the ejection pressure from 8 to 1 psi.

Figures 2, 3 and 4 are X-ray diffraction plots showing the effect of decreasing ejection pressure and consequently increasing quenching rates on the crystal structure. The tetragonal and bcc phases were diminished when the pressure decreased from 4 to 2.5 psi. (Figs. 2 and 3). At 0.9 psi the tetragonal and bcc phases were completely suppressed; there was a small amount of A-15 in a basically amorphous ductile ribbon. (Fig. 4). Table I summarizes the processing parameters.

Table I

Melt Spinning Processing Parameters for the $Ti_3Nb_6Mo_3Si_4$ Samples. Corresponding Crystal Structures are shown in Figures 2, 3, and 4.

Sample #	Wheel Speed (rpm)	Ejection Pressure (psi)	Nozzle Diameter (mm)	Thickness (mm)	Quality
1	5900	4	1	0.033	Brittle
2	5700	2.5	1	0.032	Brittle
3	5700	0.9	1	0.010	Ductile (Partly Amorphous)

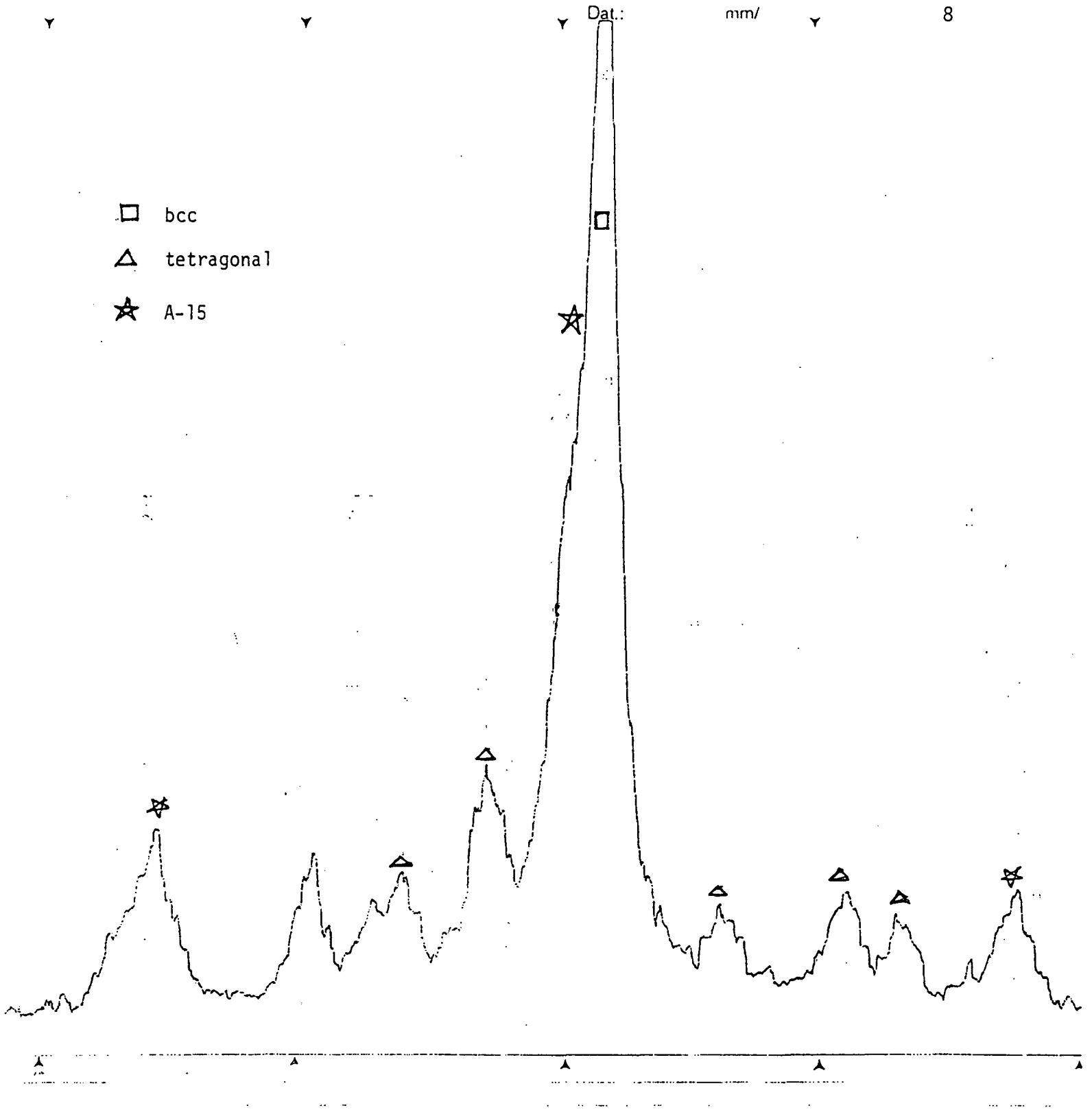

Figure 2: X-Ray Diffraction Plot of Melt Spun $Ti_3Nb_6Mo_3Si_4$
(Sample 1) (Ejection Pressure 4 psi)

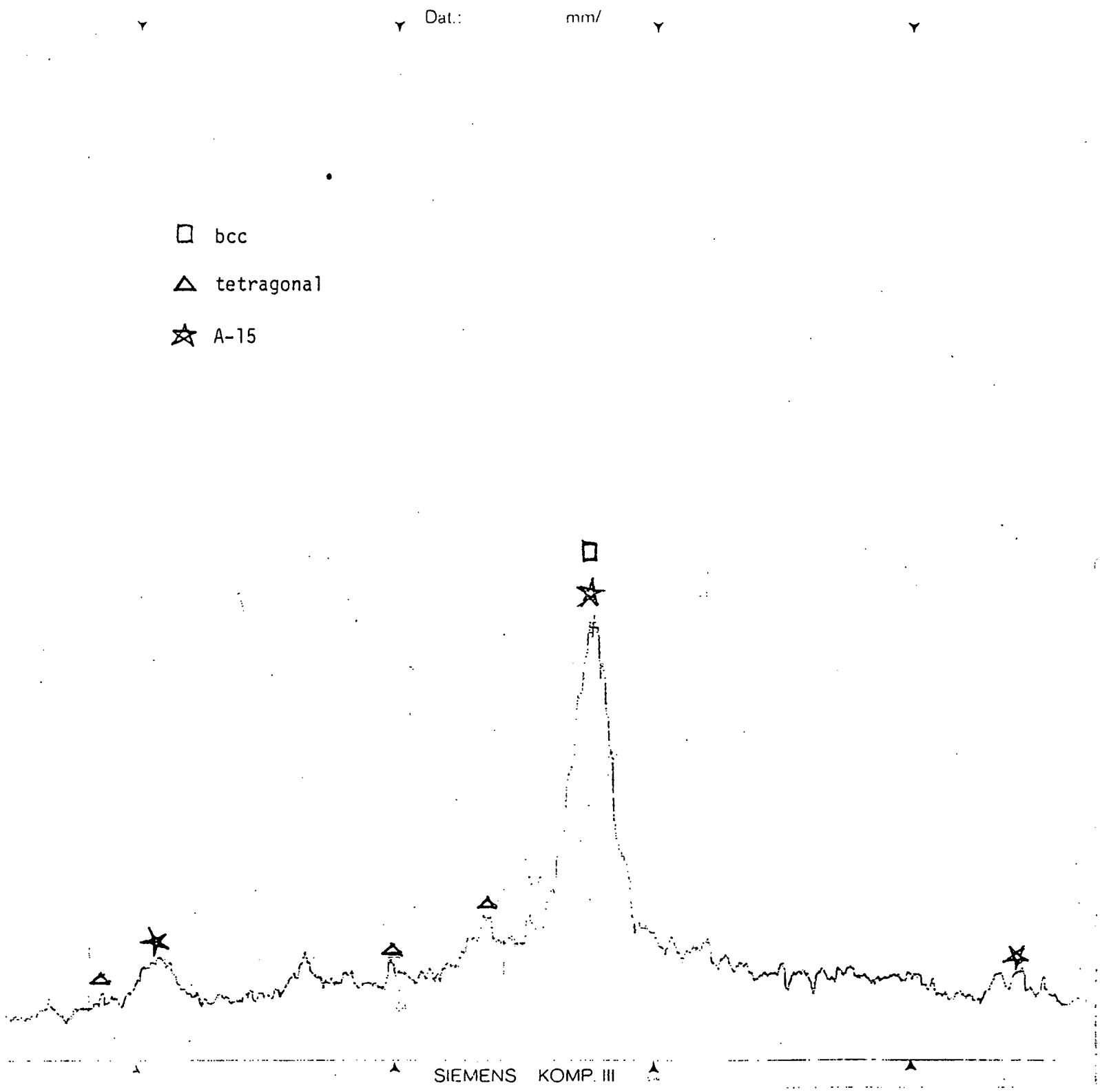

Figure 3: X-Ray Diffraction Plot of Melt Spun $Ti_3Nb_6Mo_3Si_4$ (Sample 2) (Ejection Pressure 2.5 psi)

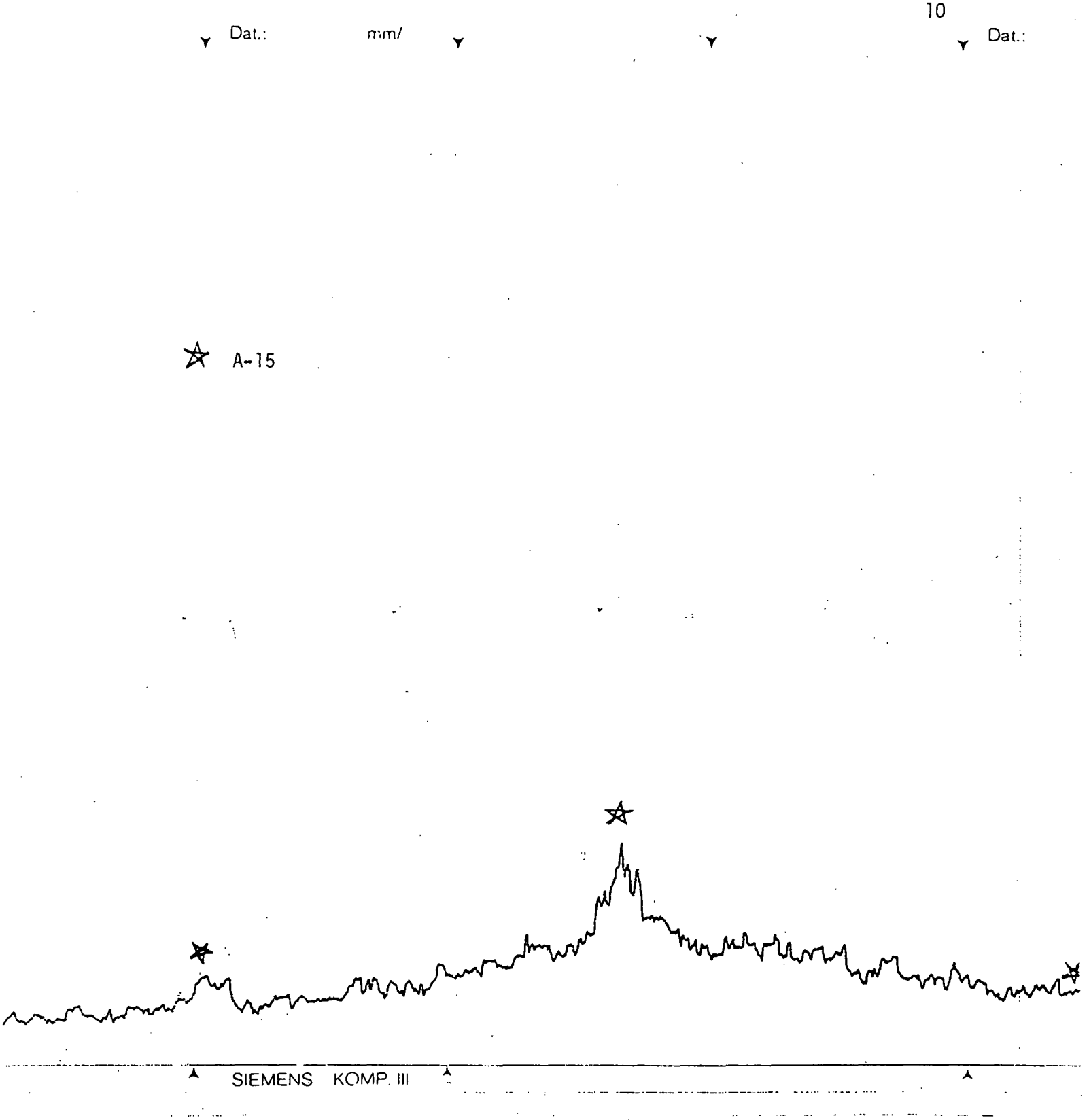

Figure 4: X-Ray Diffraction Plot of Melt Spun $Ti_3Nb_6Mo_3Si_4$
(Sample 3) (Ejection Pressure 0.9 psi)

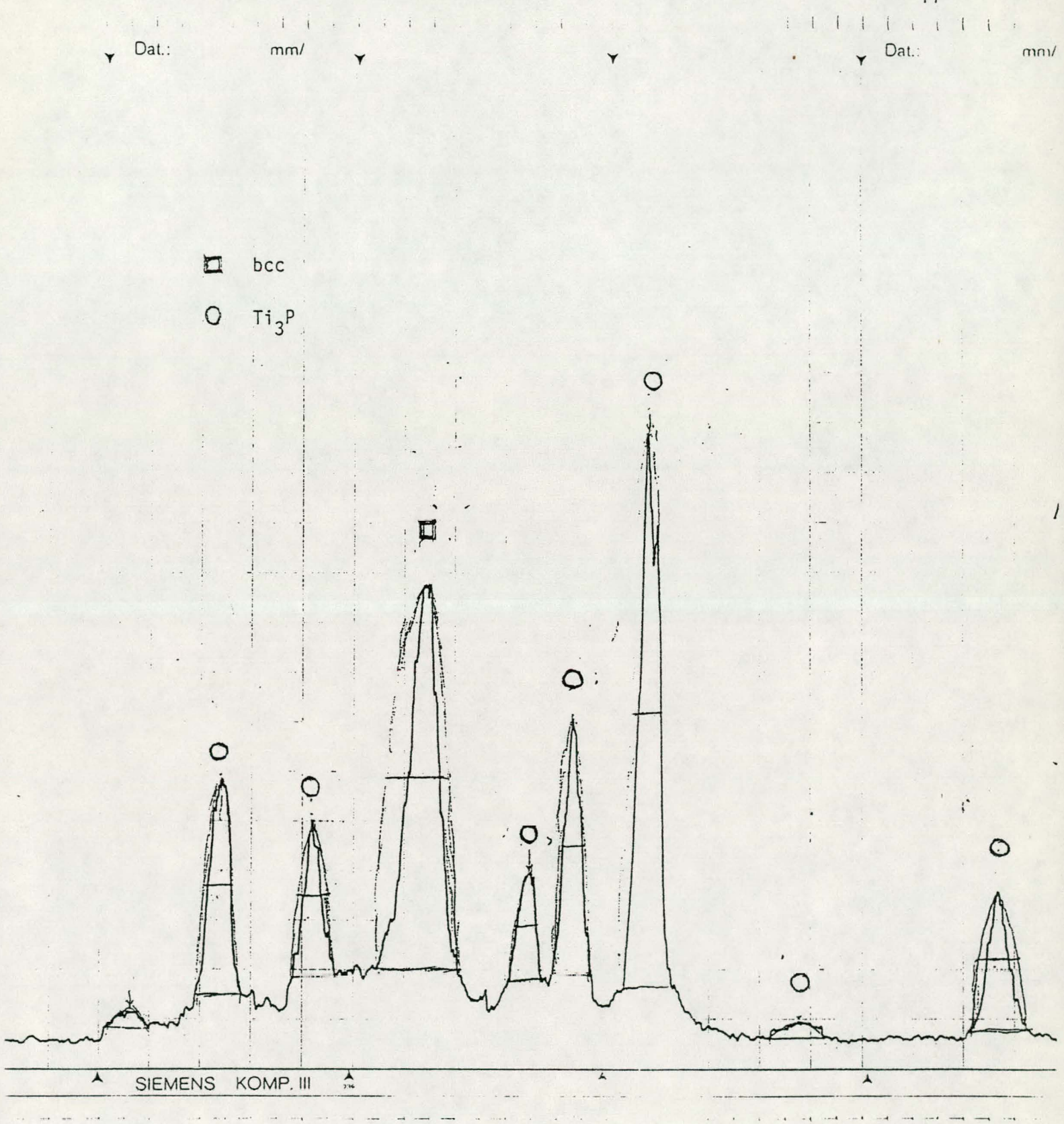

Figure 5: X-Ray Diffraction Plot of Arc Melted $Nb_{80}Si_{20}$

2. Nb_3Si and Nb_3Ge

It is thought that Niobium--Silicon, of stoichiometric composition $Nb_{75}Si_{25}$ and in the metastable A-15 crystal structure, will exhibit extremely good superconducting properties. This alloy, however, has proven to be extremely difficult to produce. One of the aims of this research project is to combine the melt spinning technique of rapid quenching with subsequent ion implantation in a novel approach to the fabrication of A-15 $Nb_{75}Si_{25}$. Following is a report of progress to date on the first part of this project--the fabrication of amorphous Nb-Si ribbons of composition as close as possible to 25 At% silicon.

The effect of quenching rates on the crystal structures of $Nb_{80}Si_{20}$ samples can be seen in the diffraction plots of Figures 5, 6, and 7. An arc melted sample showed the presence of the equilibrium Ti_3P and bcc Nb phases (Fig. 5). A melt spun partly ductile ribbon contained primarily A-15 and amorphous phases with small amounts of bcc Nb and Ti_3P phases. (Fig. 6). By further increasing the quenching rate a completely ductile amorphous ribbon was produced. (Fig. 7).

With the ongoing refinement of our technique, we have reached a point at which we can routinely produce amorphous ribbons of 19, 20 and 21 At% silicon composition. These ribbons are generally about 10 to 14 inches long, 0.5 mm. wide and 0.01 to 0.02 mm. thick. They exhibit well defined, regular edges and are very ductile. One partly ductile 21 At% silicon ribbon is particularly interesting in that its X-ray diffraction plot

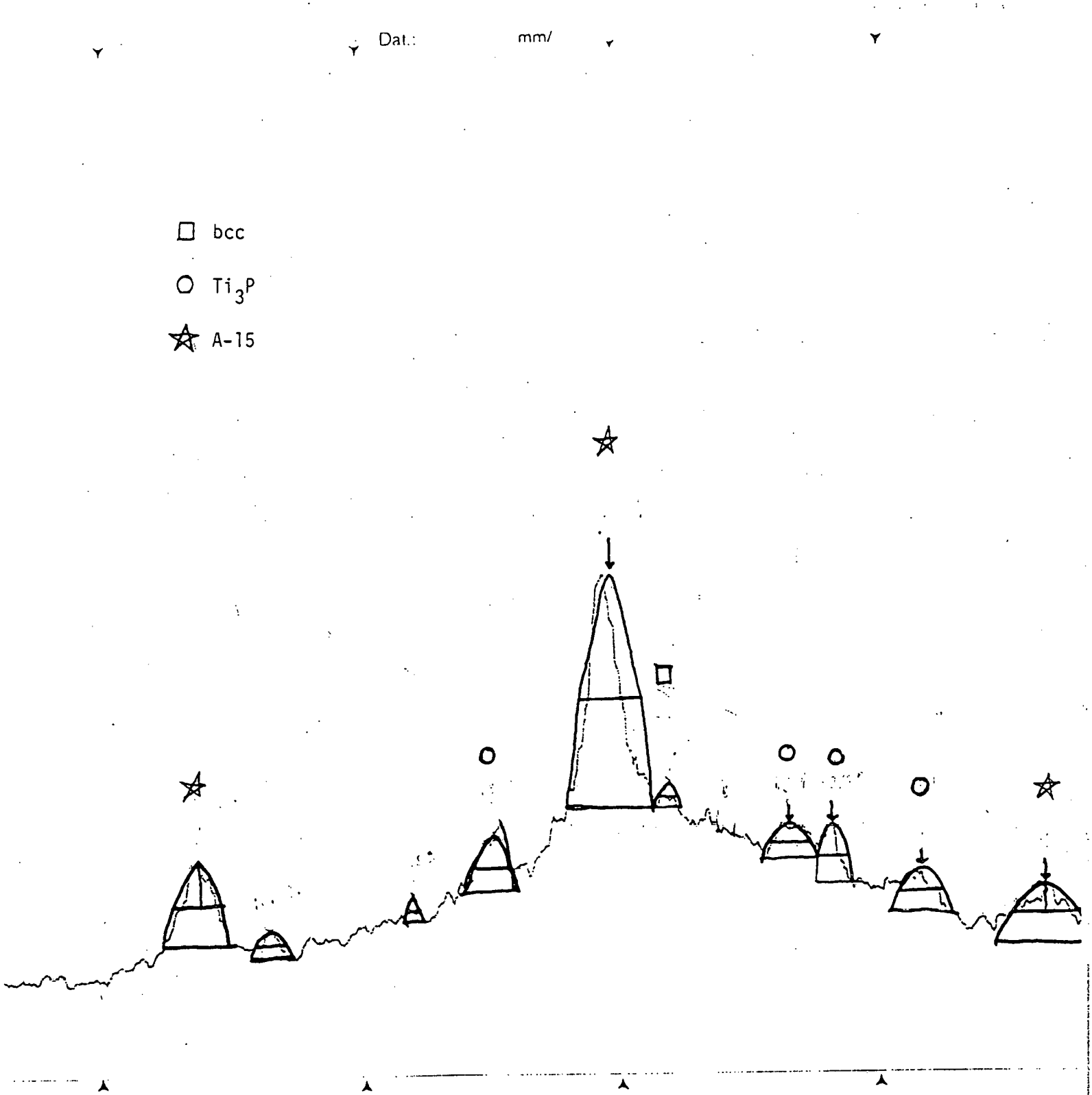

Figure 6: X-Ray Diffraction Plot of Melt Spun Partly Ductile $Nb_{80}Si_{20}$

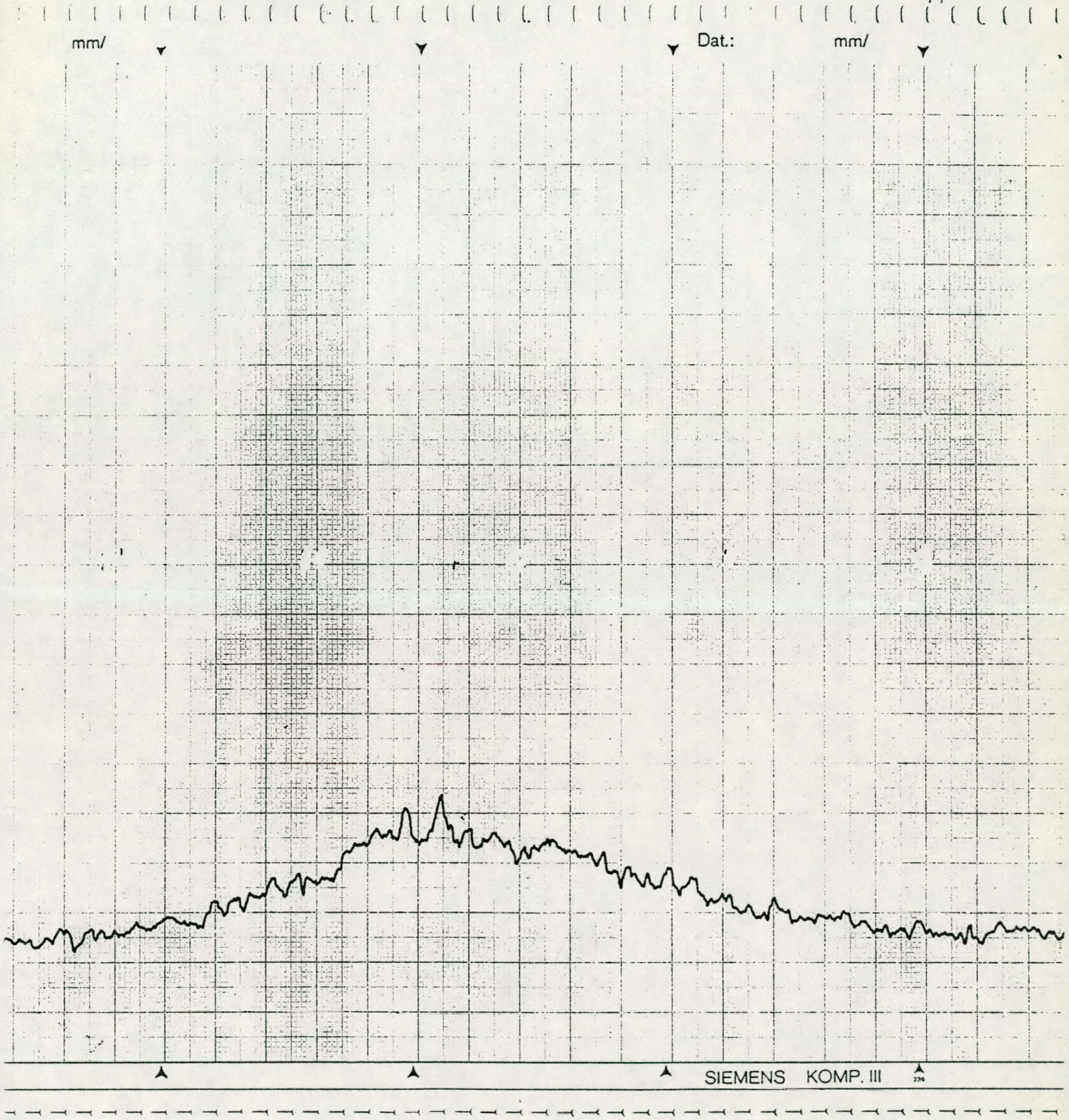

Figure 7: X-Ray Diffraction Plot of Melt Spun Very Ductile $Nb_{80}Si_{20}$

reveals the existence of amorphous and A-15 phases and the complete suppression of Ti_3P and niobium solid solution peaks. (Fig. 8).

Amorphous ribbons of 22 and 23 At% silicon are at this time still somewhat difficult to produce. Nevertheless, roughly a third of the attempts to produce amorphous ribbons in this range have been successful. Several researchers have employed melt spinning to form amorphous Nb-Si alloys. However, the highest silicon composition achieved in these efforts is reported to be 21 At% silicon. In our research we have, to date, successfully fabricated amorphous Nb-Si ribbons of composition up to and including 23 At% silicon. (Fig. 9).

Preliminary work on Niobium-Germanium alloys has revealed that these alloys are far more difficult to melt spin into ductile ribbons. However some initial success has been obtained with amorphous $Nb_{80}Ge_{20}$ alloys.

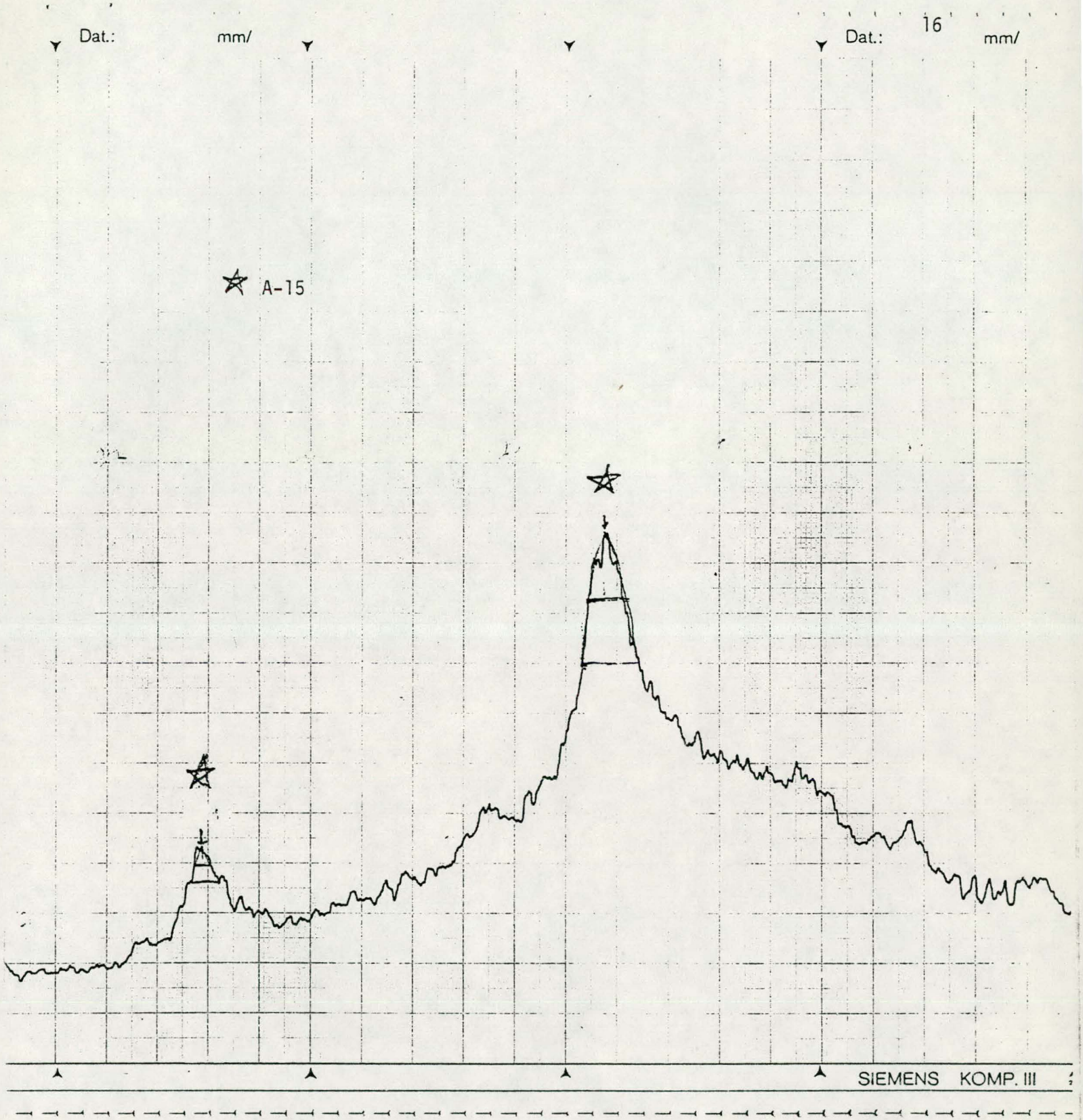

Figure 8: X-Ray Diffraction Plot of Melt Spun $Nb_{79}Si_{21}$ Showing the Existence of Amorphous and A-15 Phases and the Complete Suppression of Ti_3P and Nb Phases

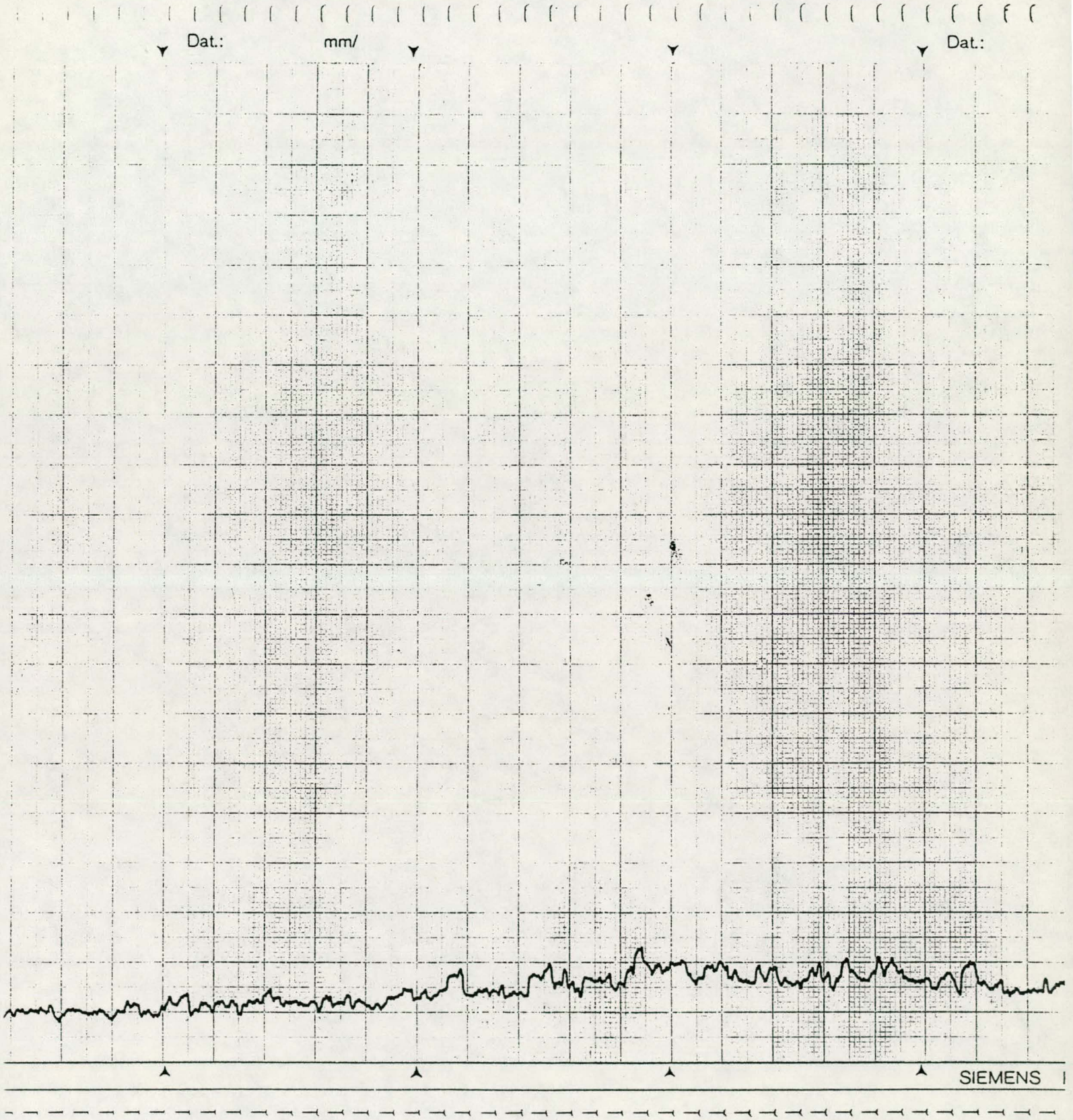

Figure 9: X-Ray Diffraction Plot of Melt Spun $Nb_{77}Si_{23}$

IV. SUMMARY AND CONCLUSIONS

The work on heavy dose implantations into A-15 substrates has been completed. (Appendix A).

The operation of the melt spinning apparatus has been optimized by designing an alloy suspension apparatus to eliminate crucible contamination and by controlling the processing parameters to obtain extremely high quenching rates.

The initial work on melt spinning of quaternaries has shown that this technique is capable of synthesizing new metastable A-15 compounds such as $(TiNbMo)_3Si$ (Appendix B) as well as amorphous alloys.

Melt spinning of niobium silicon alloys has produced single phase A-15 Nb_3Si, an extremely difficult compound to synthesize. It has also produced amorphous ductile ribbons containing up to 23 At% Si, something that has never been achieved before.

Of particular interest is that alloys containing small amounts of metastable A-15 phase in amorphous matrices have been produced ($(TiNbMo)_3Si$ and Nb_3Si)). These could serve as nucleation sites for further growth of A-15 phase during low temperature anneals.

Superconducting transition temperature measurements are currently being carried out on the melt spun alloys. Annealing and its effect on crystal structure and superconducting properties are also being studied.

The melt spinning technique is showing great promise for synthesizing new metastable A-15 compounds as well as processing them in a useable form either directly as A-15 tapes or as amorphous ribbons that can subsequently be annealed into the A-15 structure.

Appendix A

THE EFFECT OF HEAVY DOSE IMPLANTATIONS OF B AND C ON THE CRYSTAL STRUCTURE AND SUPERCONDUCTING TRANSITION TEMPERATURE OF A-15 Nb_3Al

Mireille Treuil Clapp
Department of Mechanical Engineering
University of Massachusetts
Amherst, MA 01003

The effect of ion implantation on metastable phase formation and superconducting transition temperature (T_c) has been investigated. The particular alloys studied were $Nb_3Al_{1-x}B_x$ and $Nb_3Al_{1-x}C_x$. A-15 Nb_3Al was used as the substrate material. Large doses of B and C (up to 23 At%) were implanted into Al depleted surfaces. A series of implantation energies and doses was chosen to maintain the (Al + B) and (Al + C) concentrations equal to 25 At%. This is necessary for achieving high T_c materials. Auger analysis indicated that there was very good agreement between experimental and theoretical dopant profiles immediately after implantation. After annealing up to 900°C the B atoms showed very little redistribution; however the C atoms tended to migrate towards the surface. Structural analysis using a READ camera and a diffractometer indicated that the large doses of B and C had been implanted into the A-15 structure without affecting its stability; this A-15 phase remained stable up to 950°C. Implantation caused the lattice parameter of the A-15 phase to increase by 1 to 2%. There was no increase in the superconducting transition temperature above that of the substrate (18K). This work is consistent with other studies; implantation has successfully produced metastable phases; however implantation into A-15's has not increased their T_c's.

INTRODUCTION

Ion implantation is a means of altering the surface composition of materials in a well controlled fashion. The depth of the implanted ion is a function of its energy and can range from angstroms to microns. The concentration of the implanted ion is a function of the beam current and implantation time and can vary from parts per million to tens of atomic percent. Ion implantation has been used and studied extensively in the semiconductor industry and more recently has been applied to metallurgical problems. One such application deals with the fact that ion implantation is inherently a nonequilibrium process and can be used to form metastable phases. For example, supersaturated solid solutions of Ag in Cu and W in Cu (1) have been formed; amorphous phases have been produced by heavy dose implantations (2); metastable A-15 "Nb_3Si" has been synthesized by a combination of implantation and epitaxial recrystallization (3).

The present work was concerned with the possibility of synthesizing metastable A-15 $Nb_3Al_{1-x}B_x$ and $Nb_3Al_{1-x}C_x$ by heavy dose implantations of B and C into Nb_3Al substrates. This particular system was chosen because of its superconducting properties. Nb_3Al has a high superconducting transition temperature T_c of 18 K and has the A-15 structure. Most high T_c materials seem to involve metastable materials and in particular metastable A-15's. There is empirical speculation that as the non Nb atom in the A-15 structure decreases in size, the transition temperature increases [4]. Normal alloying of B and C with Nb_3Al will make the A-15 structure unstable. Ion implantation of B and C is an interesting approach for

attempting to synthesize metastable A-15 $Nb_3Al_{1-x}B_x$ and $Nb_3Al_{1-x}C_x$ (x = 0 to 1).

The purpose of this work was therefore twofold: to further study the use of ion implantation for metastable phase formation, and to investigate the use of this technique for synthesizing high Tc metastable superconducting compounds.

EXPERIMENTAL PROCEDURE

Wafers of A-15 Nb_3Al were used as the substrate material. Their surfaces were depleted of Al by annealing in vacuum. The Al deficiency was then replaced with B or C ions by implanting at a sequence of energies and doses. The composition of the implanted layer thus changed gradually from the bulk Nb_3Al to $Nb_3(Al + B)$ and finally to Nb_3B at the immediate surface. A similar composition profile was obtained for Nb_3C. Different implantation energies and doses were used so that the (Al + B) or (Al + C) concentrations could remain equal to the desirable stoichiometric composition of 25 At% throughout the entire implanted layer. This is necessary for achieving high T_c materials. Indeed it has been observed that T_c is highest in well ordered stoichiometric compounds [4]. The compositions and dopant profiles of the implanted layers were determined using Auger analysis. The structures were analyzed with a diffractometer and a READ X-Ray camera. The superconducting transition temperatures were measured using a four point probe resistive technique.

Sample Preparation: For the ion implantation experiments, finely polished slices of A-15 Nb_3Al were required. These were prepared from high purity elemental powders (Nb, 99.8% metallic purity, and Al, 99.8% metallic purity, 99% total purity) that were compacted under high pressure and arc melted in a titanium gettered argon atmosphere, using a nonconsumable tungsten electrode. They were homogenized at 1840°C for two hours, and ordered at 750°C for two days. The samples then had a T_c of 18°K. They were primarily A-15; some contained a very small amount of phase; no bcc

Nb was present. They were sliced, finely polished (1/4 micron diamond paste) and lightly etched.

In order to remove Al from the samples' surface, they were heat treated in a dynamic vacuum furnace at temperatures above 1000°C for several hours. During this process the Al evaporated off the surface and diffused out of the interior of the sample. The diffusion profile was calculated from equation (1):

$$C(x, t) = C_o \, \mathrm{erf}\left(\frac{x}{2\,(Dt)^{1/2}}\right) \qquad (1)$$

where $C(x, t)$ is the concentration at time t and distance x, C_o is the initial concentration, D is the diffusion coefficient of Al in Nb_3Al, and is equal to (5):

$$D = 2.4 \exp(-86000/RT)$$

A typical calculated diffusion profile after six hours at 1060°C is shown in Figure 1.

Ion Implantation: Once the Al had been diffused out of the samples, it was necessary to replace it with B or C in such a way that the $Al_{1-x}B_x$ or $Al_{1-x}C_x$ remained equal to 25 At%, over the entire Al depleted volume. This was attempted by choosing a variety of implantation energies and doses. One of the main reasons for producing uniform implanted layers was for using X-ray diffraction analysis. Two implantation conditions were investigated. First, the ions were accelerated to relatively low energies,

ranging from 30 keV to 160 keV; their maximum penetration depth was of the order of .75 microns; both C and B ions were implanted, but separately into different samples. Second, the ions were accelerated to much higher energies, up to 1 MeV; their maximum penetration depth was of the order of 2.5 microns; only B ions were implanted for reasons that will be explained later.

Values of penetration depth Rp, and range straggling Δ Rp were calculated from Lindhard, Scharff and Schiott theory (6) for a variety of energies for B and C ions implanted into Nb and are listed in Table I. With the ion dose known, it is possible to calculate the concentrations of B and C in atomic percent for the $Nb_3Al_{1-x}B_x$ and $Nb_3Al_{1-x}C_x$ compounds. Figures 2 and 3 show the individual ion dopant profiles as well as the cumulative ones. By comparing the cumulative concentrations with the Al depletion profiles, it can be seen that the calculated (Al + B) and (Al + C) values remained close to the desirable stoichiometric value of 25 At% at practically all depths into the implanted layer. Implantations were carried out on a Cockcraft Walton accelerator that had an energy range of 30 to 160 keV and could provide high current densities (7). During implantation samples were kept in a vacuum of 10^{-6} torr.

High energy implants with B: A deeper layer of Al was diffused out of the samples by heating in vacuum at $1100^{o}C$ for 25 hours. The resultant calculated Al depletion profile is shown in Figure 4. Boron was implanted at seven different energies and doses as listed in Table II. The cumulative dopant profile is shown in Figure 4. It can be seen that the missing

Al was replaced by B in such a way that the (Al +B) composition remained close to 25 At%. The two highest energies were carried out on a Van der Graff accelerator with low beam currents (8). The other energies were obtained on a commercial implanter (9) that had high beam currents; however, the highest energy available was 200 KeV so for the 400 KeV and 320 KeV runs, doubly ionized B^{++} beams of 200 and 160 KeV were used.

Heat Treatments of Implanted Layers: Ion implantation invariably produces radiation damage, resulting in a disordered surface layer with defects. It is possible to reorder the surface or remove the defects by heat treatments. Three methods were investigated, furnace annealing, electron beam annealing and electron beam melting.

The implanted samples were subjected to 24 hour ordering anneals in a dynamic vacuum furnace in $50^{o}C$ steps up to $1000^{o}C$.

The effect of electron beam annealing on the implanted layers was studied. The e beam parameters were adjusted to maintain the surface temperature slightly below the liquidus and are listed in Table III (10). To limit the diffusion of the small B and C atoms an intense pulse of short duration was required. For the C implanted samples high power density and a few pulses worked well. However the B implanted samples cracked under these conditions and a lower power density and more pulses were used. It was assumed that this was because the larger B atoms had strained the surfaces more than the C atoms, making them less resistant to thermal shock. The samples were then subjected to an ordering anneal at $700^{o}C$ for 24 hours.

Samples were also subjected to a more powerful e beam in order to study the effects of melting the surface. However when the melted surface solidified, it flaked off the substrate and a brittle powdery film was obtained.

Compositional Analysis: Surface concentration profiles were determined experimentally using Auger analysis. By sputtering with an argon beam successive atomic layers were removed and the intensities of the Auger peaks were measured as a function of sputtering time. Since peak intensity can vary not only with the elements but also with their surrounding matrix, standard samples were prepared for purposes of converting intensity to atomic percent. A series of $Nb_3Al_{1-x}B_x$ and $Nb_3Al_{1-x}C_x$ samples were analyzed with x equal to 0, .25, .5, .75 and 1. Sputtering time was converted to distance by measuring the time required to sputter away layers of known depth on standard samples. Composition profiles of Nb, Al, B and C as a function of depth were thus obtained. Auger peaks of the following energies were chosen for analysis: 1944eV Nb peak, 1378eV Al peak, 272eV C peak and 179eV B peak. Since there is a strong Nb peak at 167eV, care was taken to prevent its signal from interfering with the B signal. This was achieved by picking a narrow energy range skewed toward high values for the B signal.

Superconducting transition temperature measurements: The superconducting transitions were measured between $4.2^{o}K$ and $25^{o}K$ using a four point probe resistive technique. Temperature was determined with a calibrated Ge resistance thermometer. Accuracy was verified by measuring

standard samples of Nb and Nb_3Al of known Tc. The samples consisted of a substrate material with a T_c of 18^oK, on top of which was an implanted layer of unknown T_c. Two possibilities could have existed.

a) T_c (implanted layer) > T_c (substrate)

In this case as soon as T_c (implanted layer) was reached, the surface layer would act as a shunt and there would be a large drop in voltage that would easily be detected. Exceeding the critical current density J_c could be a problem in this case so current through the sample was kept to a minimum. Typical sample dimensions were 1 cm x 0.5 cm x 0.05 cm. The implanted layer was approximately 1 micron deep and 0.5 cm wide. Currents of 1 m Amp were used giving a current density for the implanted layer of 20 Amps/cm^2. Typical J_c's for Nb_3Al near T_c are greater than 100 Amps/cm^2.

b) T_c (implanted layer) < T_c (substrate)

In this case there would be a large drop in voltage at T_c (substrate), followed by a much smaller drop at T_c (implanted layer). In order to detect such a small second transition a nanovoltmeter was used. To verify the possibility of observing such a transition, a layer of lead (T_c 7k) several hundred angstroms thick was deposited on a Nb substrate (T_c 9k); Two lead configurations were used. The first consisted of placing the two current and two voltage leads directly on the implanted surface layer. The second consisted of placing the leads on the front and back of the sample in such a way that the current was passing perpendicular to the surface; there were effectively two resistances in series. With the nanovoltmeter, the superconducting transition of the lead surface layer was detectable.

Structural Analysis: X-Ray diffraction was used to analyze the structure of the implanted layers both in terms of phase determination and lattice parameter (a_0) measurement. Of particular interest was establishing whether or not the surface had the A-15 structure after heavy dose implantation and annealing. Since the substrate material was A-15, it was necessary to assure that the X-Rays were sampling the implanted layer and not the substrate. This would be accomplished if the X-radiation were absorbed before it reached the substrate.

Of the commonly available X-ray sources, Cr is the most strongly absorbed by Nb. Penetration depths for 90% absorption as a function of angle of incidence θ were calculated from the linear absorption equation for X-rays and are listed in Table (IV). It was necessary that these penetration depths be smaller than the thickness of the implanted layers. The low energy and high energy implants had implanted layers 0.75 and 2.5 microns deep respectively. The low energy implants were therefore analyzed with a READ X-Ray camera: in this camera, the X-Ray beam has a small θ which is kept constant and which was fixed at 7^{o}. The high energy implants could be analyzed with both the READ camera and an X-Ray diffractometer where θ was allowed to scan from 15 to 40^{o}. Cr radiation was used in all cases.

Since the X-Rays were diffracted off a solid flat surface rather than a powdered specimen, rotating sample holders for both the diffractometer and the READ camera were built to randomize the diffracted intensities.

RESULTS

Compositional Analysis: Samples were Auger analyzed after implanting and after annealing at successive temperatures up to 900°C. Composition profiles of Nb, Al, B and C were measured as a function of depth into the sample. The Auger analysis done immediately after implantation showed very good agreement between the theoretically and experimentally determined dopant profiles. The effect of annealing on the implanted species can be seen in Figures (5) and (6) and Tables (V) and (VI) for B and C respectively. Figure (5) is a plot of Auger peak intensities of B and Al versus depth into a B implanted sample after annealing at 850°C for 24 hours. Table (V) shows a comparison of these results with the theoretical values. By comparing the ratios of B(At%) to Al(At%) for theory and experiment (columns 4 and 8), it can be seen that there is good agreement. This means that there has been little redistribution of the implanted B ions after annealing. Figure (6) is an Auger depth profile for C and Al after annealing a C implanted sample at 805°C for 24 hours. In this case agreement between experiment and theory is not as good; there is a higher concentration of C near the surface of the sample after annealing. The difference in behavior of the B and C implanted samples can be attributed to enhanced diffusion of the smaller C atom. For this reason the high energy implants were only carried out with B ions.

Structural Analysis: Structural analysis of the samples implanted with high energy B ions was done before and after implantation and after the following heat treatments: 300, 500, 650, 730, 800, 850, 900, 950, 1000 and 1050°C for 4 hours each. The results are listed in Table VII. After the Al depletion anneal, the surfaces were two phase, bcc Nb and A-15 Nb_3Al. This is consistent with the Nb-Al phase diagram. After the B implantations the same two phases were observed. This meant that the very high doses of B (up to 23 At%) were randomly distributed in the bcc and A-15 phases. However the lattice parameter a_o of the A-15 phase increased by 2% and remained so even after annealing. Disorder due to implantation is normally annealed out. It is therefore probable that the lattice expansion was due to having some of the small B atoms having positioned themselves interstitially. The structure remained stable up to 900°C. At 950°C the Nb_3B_2 phase began to precipitate out; it grew with increase in temperature primarily at the expense of the Nb phase. Additional information was obtained with the READ camera. Up to 1000°C the A-15 lines were fine and continuous; at 1050°C they began to separate into an array of fine spots, indicating that a significant amount of texture had resulted from the annealing; certain A-15 grains were growing at the expense of others possibly due to epitaxial influence of the substrate. The samples implanted with low energy B ions differed from the high energy implants in that the lattice parameter of the A-15 phase was only increased by 1%. In this case the total ion dose was considerably less (3.7×10^{17} ions/cm^2 as compared to 11.0×10^{17} ions/cm^2). Therefore the number of interstitial B atoms was fewer causing less expansion of the lattice. The low energy C

implantations increased a_o by only 0.5%, the smaller C atom having caused less lattice expansion. Electron beam annealing did not alter the crystal structure. However the resulting thermal disorder and strain caused a_o of the A-15 phase to further increase by one percent. A summary of the effect of implantation conditions and heat treatments on the A-15 lattice parameter is given in Table VIII. The effects of increasing ion dose, atom size and thermal strain were cumulative and all contributed to an increase in a_o.

Superconducting Transition Temperature Measurements. No increase in T_c above that of the substrate was observed. It was also not possible to detect a small second transition below T_c (substrate). This meant that T_c (implanted layer) was either below 4.2°K, or that its transition had been broadened by the large dose implantations, making it undetectable with the nanovoltmeter.

SUMMARY AND CONCLUSIONS

Very large doses of B (up to 11.0×10^{17} ions/cm^2) and C (up to 3.6×10^{17} ions/cm^2) were implanted into "Nb_3Al" substrates. Extremely good agreement was obtained between theoretical and experimental dopant profiles. Ion implantation with low atomic number elements can therefore be used to accurately modify in significant amounts (23 At% in this study) the surface composition of alloys. The distribution of B was not affected by annealing up to 900°C; the C had a slight tendency to diffuse towards the surface.

Implantation did not change the crystal structure of the alloys. This is in agreement with lower dose implantation experiments where structural stability was found to be maintained (1). However the stability involving the very high doses used in our experiments is remarkable.

The lattice parameter a_o of the A-15 phase was increased, most probably due to interstitial B and C; a_o increased proportionally to the dose, 2% for the higher energy and dose B implantations and 1% for the lower energy and dose implantations. The larger B ions strained the lattice more than the smaller C ions. This was further verified by the electron beam annealing experiments; the B implanted samples cracked more easily. Electron beam annealing did not affect the stability of the A-15 phase but it further increased a_o by 1%.

There was no increase in the superconducting transition temperature of the alloy above that of the substrate. This is consistent with the observed increase in a_o. For a given alloy system, it is necessary to decrease a_o in order to increase T_c; this is because there is a rapproche-

ment of the Nb atoms and an increase in the electronic density of states. Previous work on Tc of ion implanted A-15s has shown similar results. Ion implantation of large doses of Si into A-15 substrates produced metastable A-15 Nb_3Si but with a low T_c of 5.6K. (3) Carbon implantation into A-15 Vanadium Silicon alloys showed that 5 At% C was incorporated into the A-15 structure; implantation caused a nonstoichiometric low T_c alloy of 8K to increase to 17K (11); however T_c was never found to increase above 17K, the T_c for normally processed A-15 V_3Si. Germanium implantation into nonstoichiometric A-15 "Nb_3Ge" increased T_c from 6.5 to 16.2K (12), a considerably lower value than the T_c of 23K for sputtered A-15 Nb_3Ge.

References

1. J.A. Borders, J.M. Poate, Phys. Rev. B 13: 969-79 (1976).
2. J.A. Borders, Annual Review of Materials Science 9, 325-333 (1979).
3. M.T. Clapp, R.M. Rose, J. Appl. Phys. 51 (1), 540-544 (1980).
4. Dew Hughes, D Cryogenics, 435-454 (1975).
5. A. Vignes Slama, J Less. Comm. Met., 29 (1972).
6. J.W. Mayer, L. Eriksson, J.A. Davies, "Ion Implantation in Semiconductors", Academic Press, New York & London (1970).
7. Courtesy of H. Hayden, Phys. Dept. Univ. of Conn., Storrs.
8. Courtesy of Q. Kessel, Phys. Dept. Univ. of Conn., Storrs.
9. Courtesy of B. Cordtz, Varian Assocs., Gloucester, MA.
10. Courtesy of B. Lewis, Metallurgy Dept. Univ. of Conn., Storrs.
11. J.R. Gavaler, A.I. Braginski, A.S. Manocha, B.R. Appleton, C.W. White, J.M. Williams, Procs. Matls. Res. Soc., 7, 287-93 (1982).
12. J. Geerk, Solid State Commun., 33, 7, 761-764 (1980).

This research was supported by the Department of Energy under contract No. DEAC0280ER10566.A003

List of Figures

Fig. 1

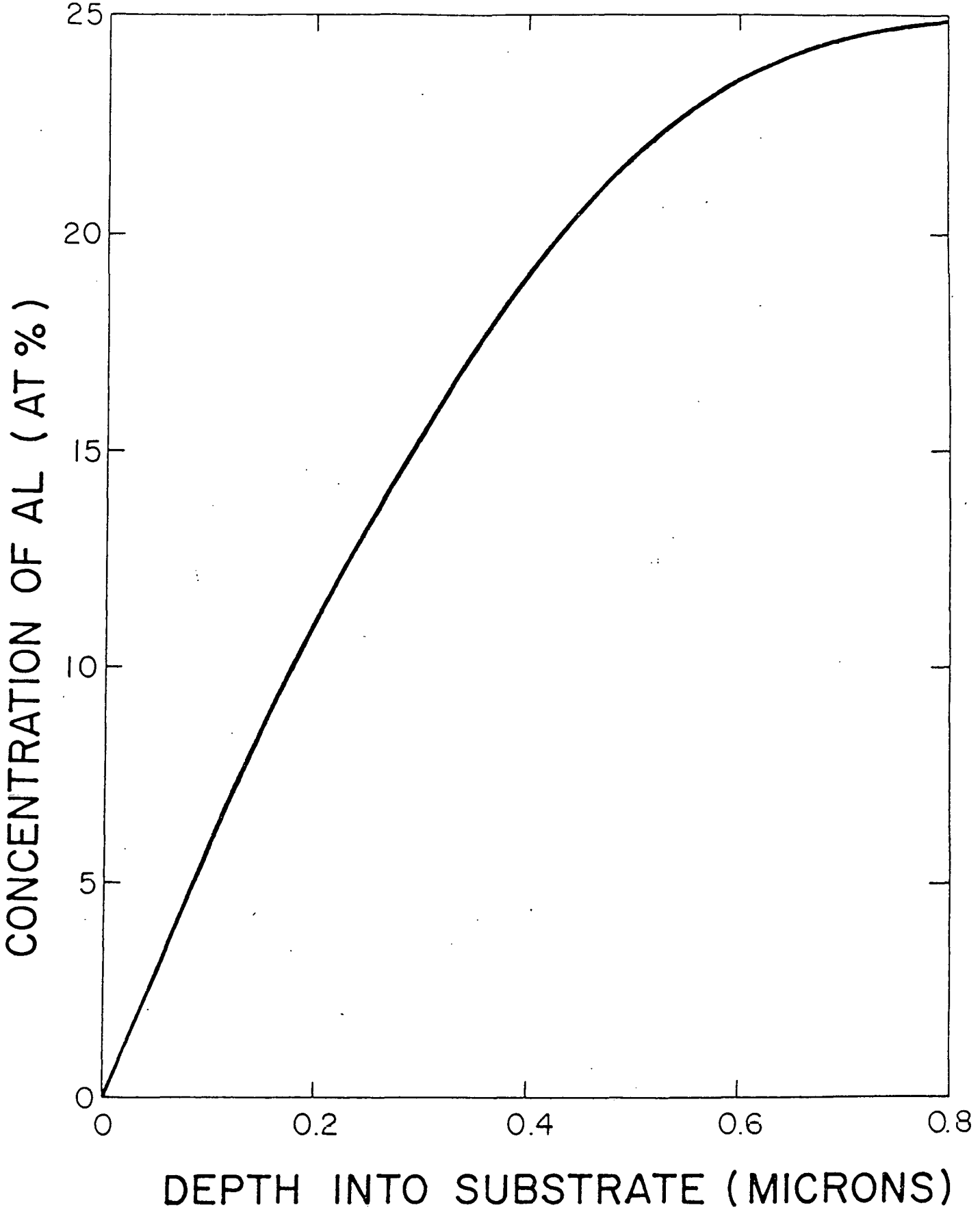
25
20
15
10
5
0
CONCENTRATION OF AL (AT %)
0
0.2
0.4
0.6
0.8
DEPTH INTO SUBSTRATE (MICRONS)

Fig. 2

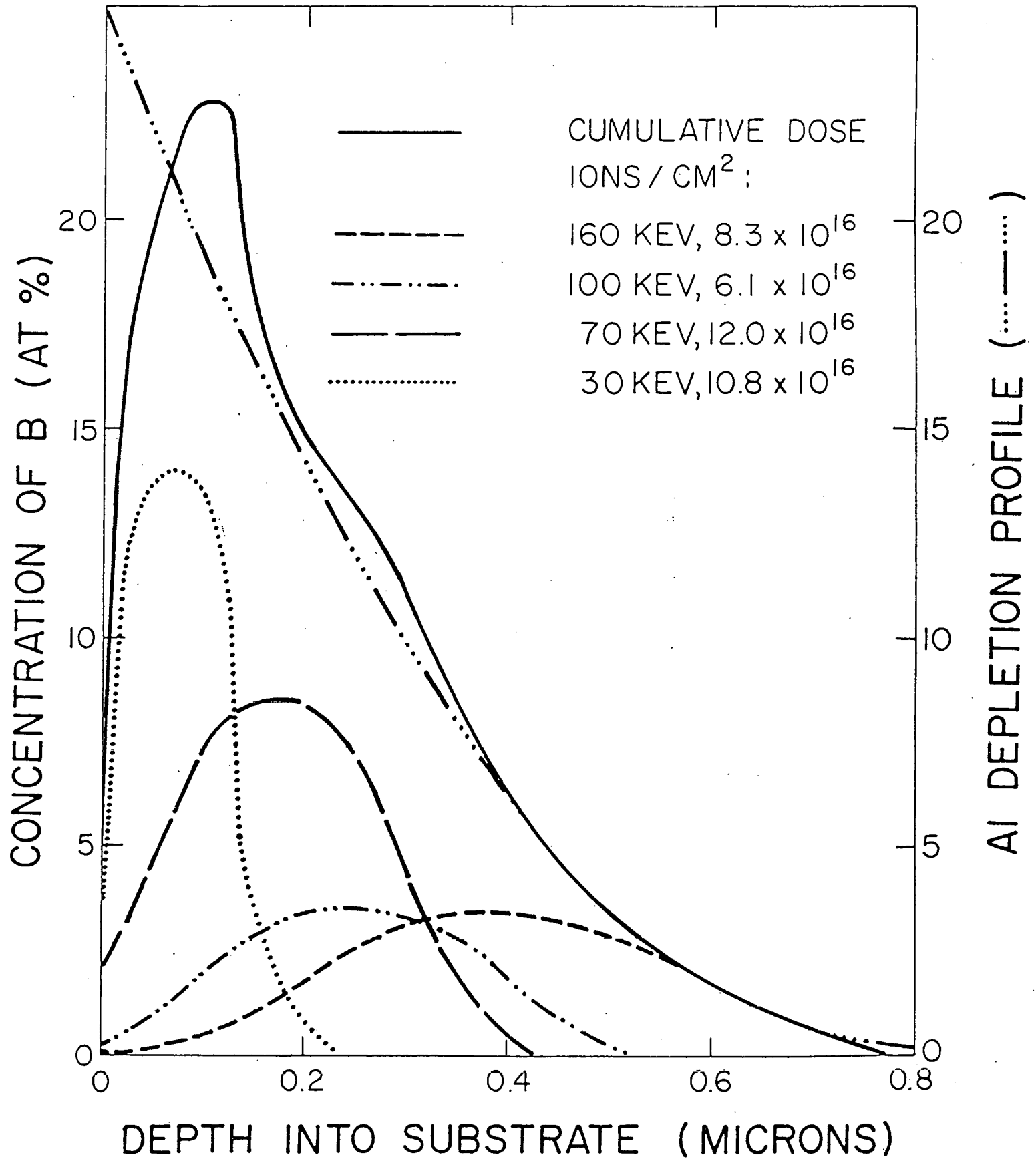
CUMULATIVE DOSE
IONS / CM^2 :
160 KEV, 8.3 x 10^{16}
100 KEV, 6.1 x 10^{16}
70 KEV, 12.0 x 10^{16}
30 KEV, 10.8 x 10^{16}
CONCENTRATION OF B (AT %)
Al DEPLETION PROFILE (.....——.....)
DEPTH INTO SUBSTRATE (MICRONS)
0
5
10
15
20
0.2
0.4
0.6
0.8

Fig. 3

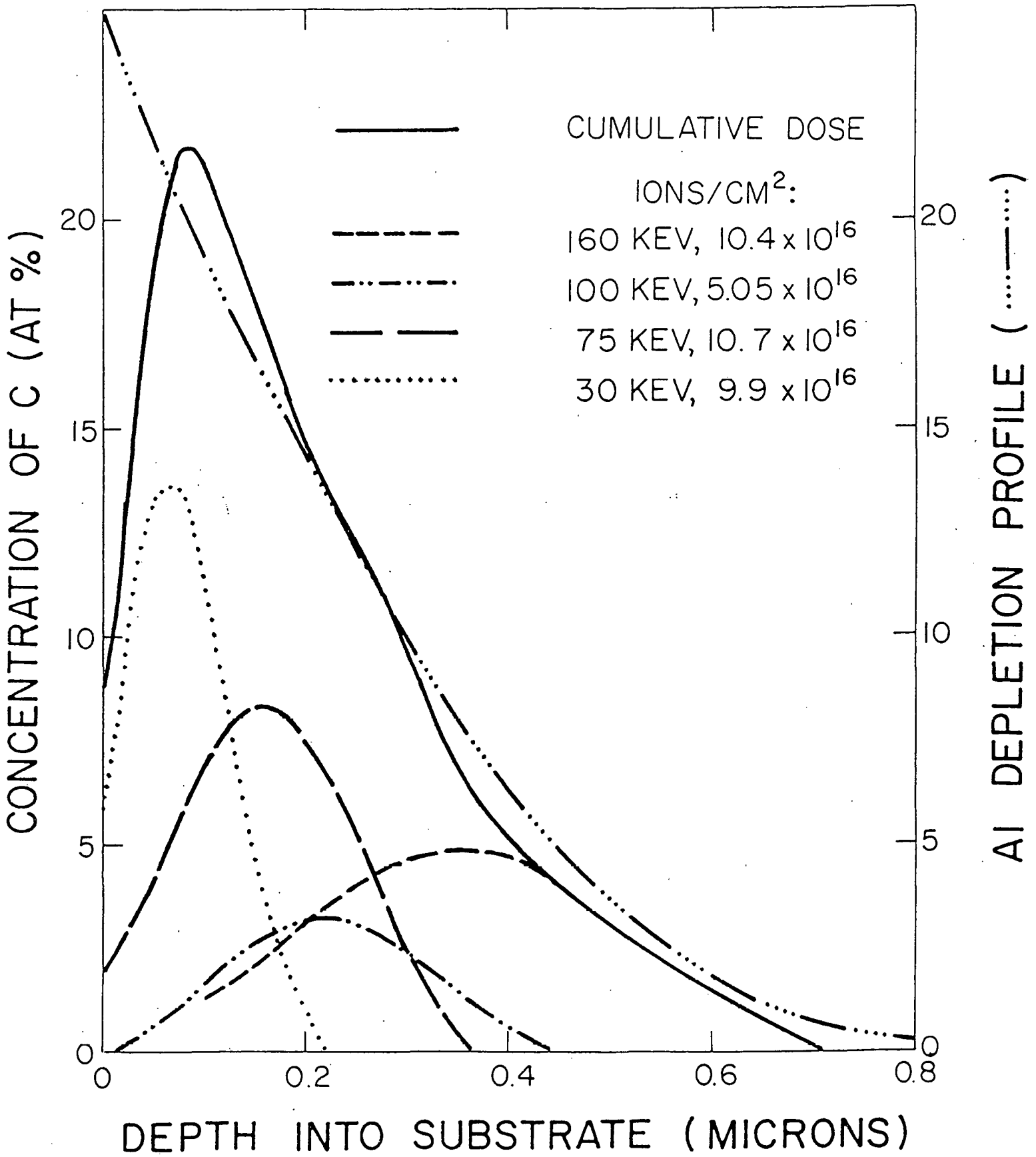
CUMULATIVE DOSE
IONS/CM²:
160 KEV, 10.4 x 10¹⁶
100 KEV, 5.05 x 10¹⁶
75 KEV, 10.7 x 10¹⁶
30 KEV, 9.9 x 10¹⁶
CONCENTRATION OF C (AT %)
Al DEPLETION PROFILE (.....——.....)
DEPTH INTO SUBSTRATE (MICRONS)
0
5
10
15
20
0.2
0.4
0.6
0.8

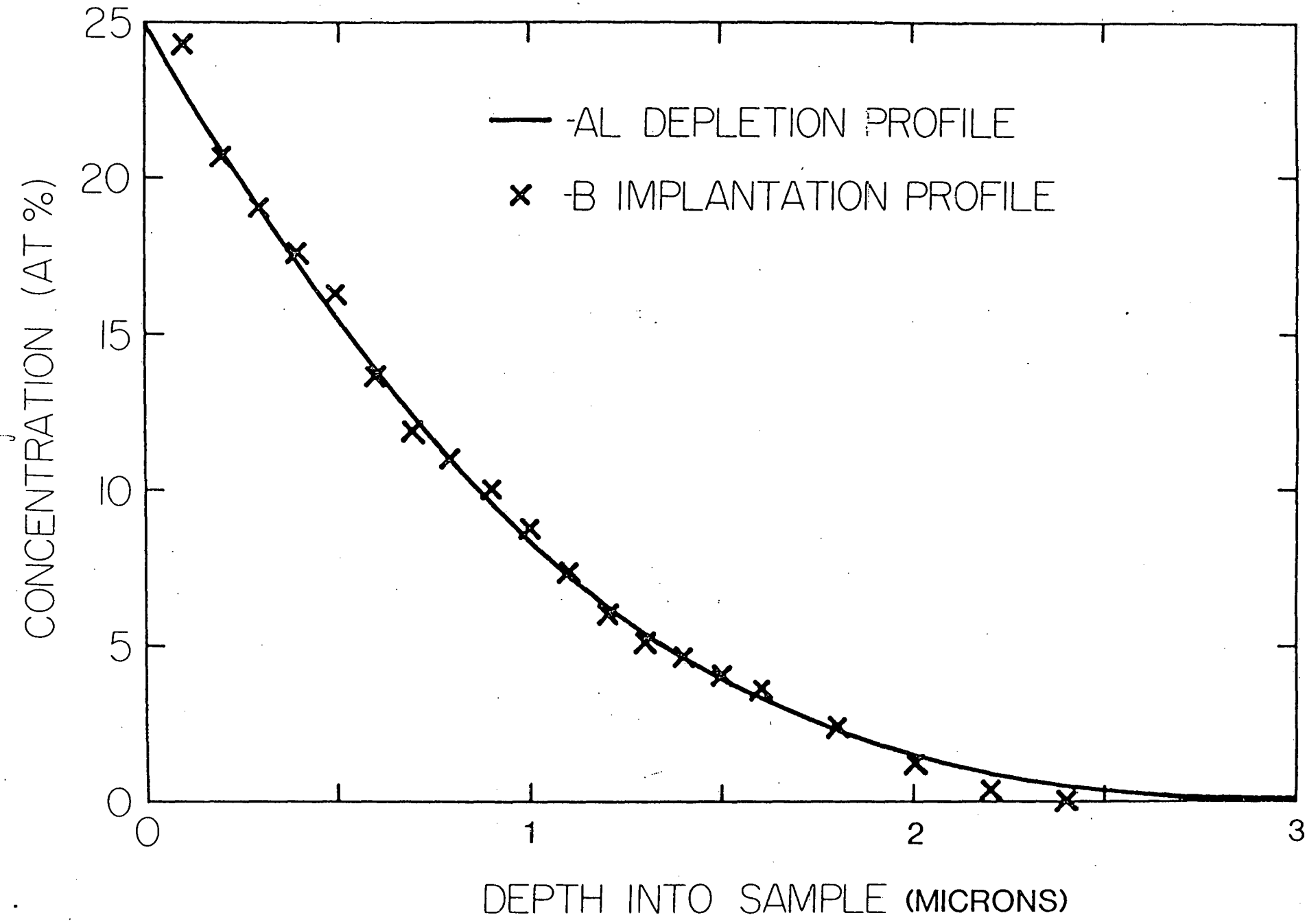
25
20
15
10
5
0
0
1
2
3
CONCENTRATION (AT %)
DEPTH INTO SAMPLE (MICRONS)
-AL DEPLETION PROFILE
-B IMPLANTATION PROFILE

Fig. 5

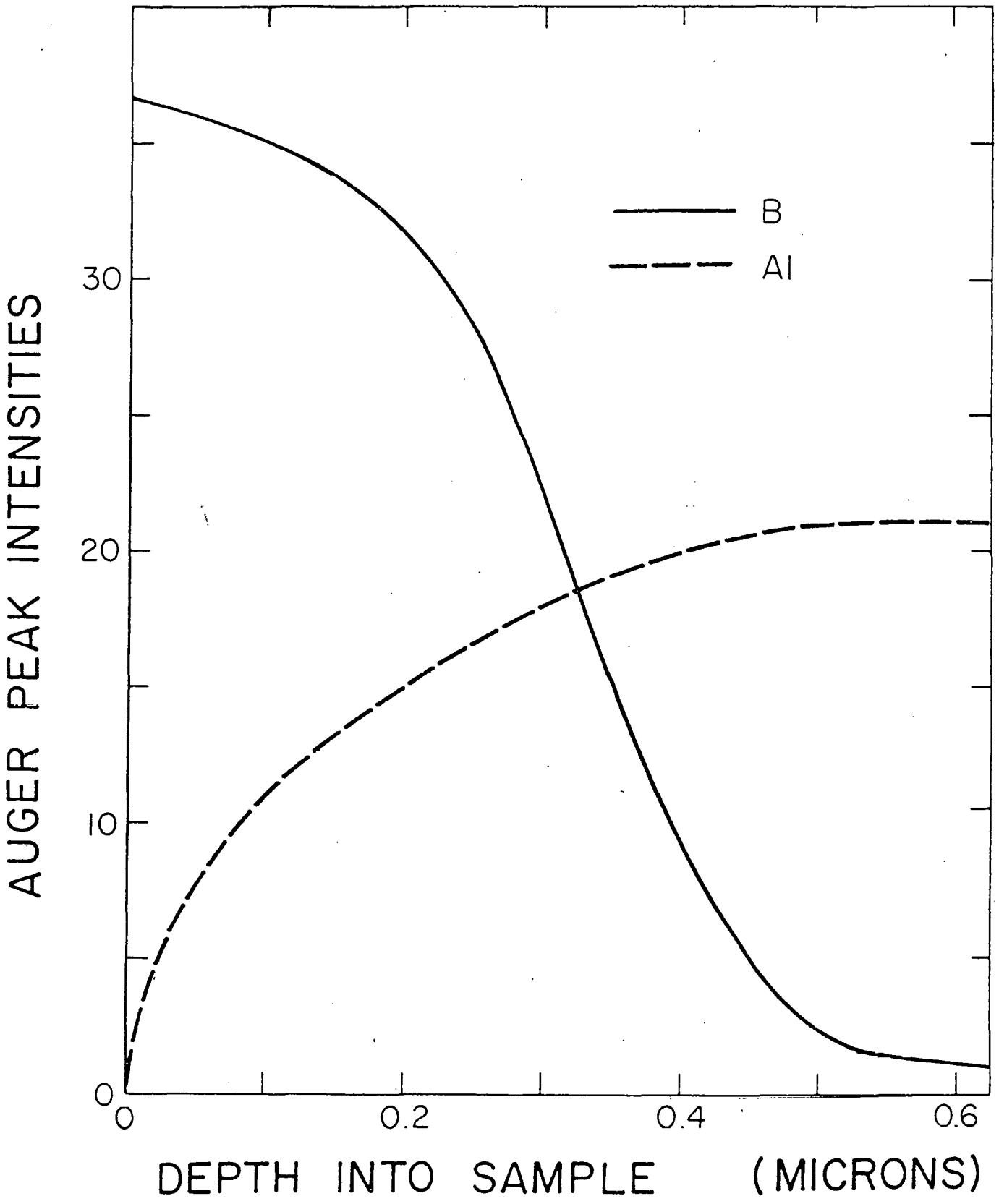
B
Al
AUGER PEAK INTENSITIES
30
20
10
0
0
0.2
0.4
0.6
DEPTH INTO SAMPLE (MICRONS)

Fig. 6

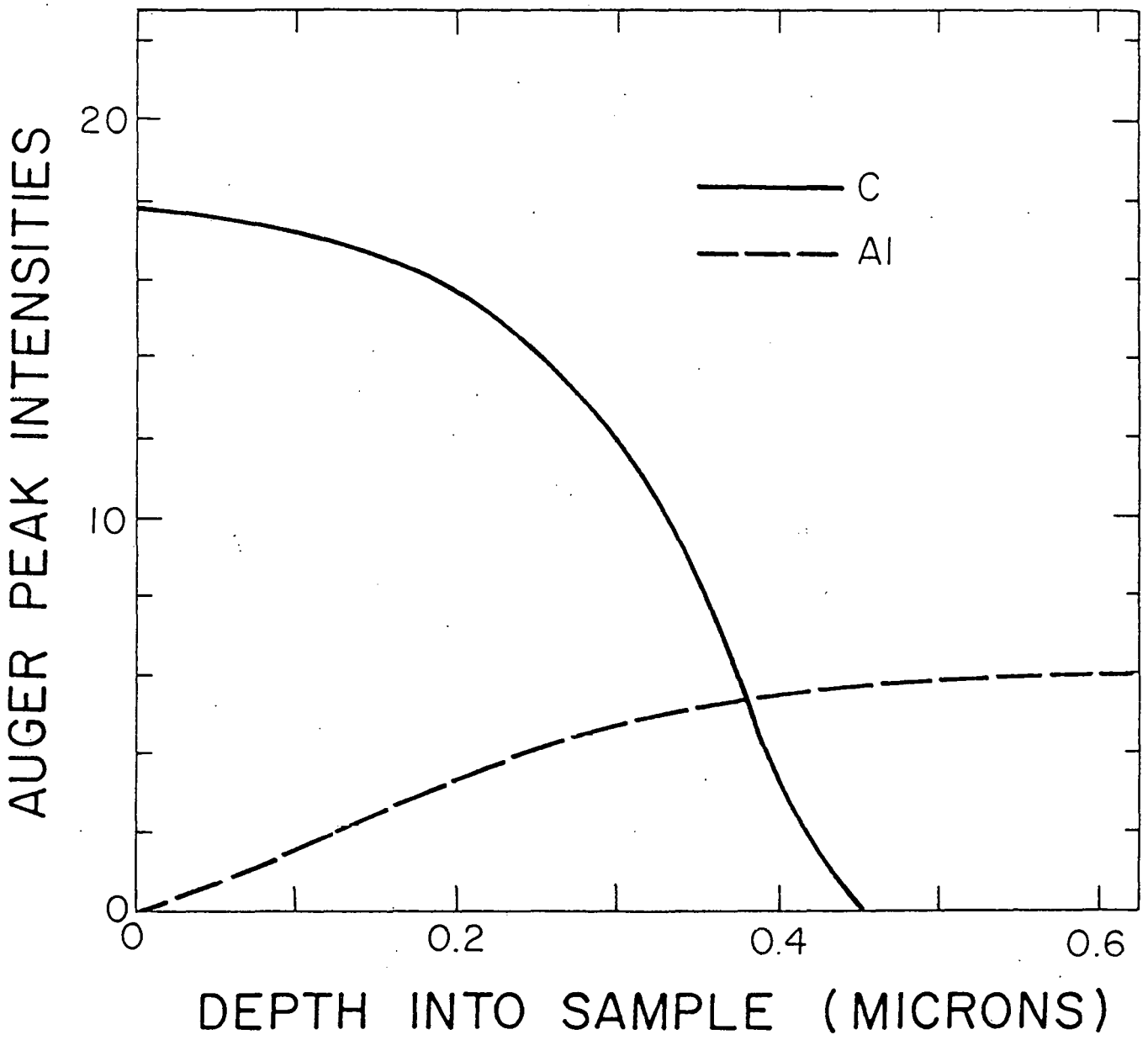
AUGER PEAK INTENSITIES
20
10
0
0
0.2
0.4
0.6
C
Al
DEPTH INTO SAMPLE (MICRONS)

Table I

Values of penetration depths R_p and range distribution ΔR_p for B and C ions implanted into Nb substrates.

ion beam energy Kev	R_p microns	ΔR_p microns
	B+ ions	
160	0.4000	0.1760
100	0.2500	0.1300
90	0.2250	0.1210
80	0.2000	0.1120
70	0.1750	0.1050
30	0.0750	0.0570
	C+ ions	
160	0.3500	0.1540
100	0.2200	0.1145
90	0.1950	0.1055
80	0.1700	0.0950
70	0.1500	0.0900
30	0.0700	0.0530

Table II

Energies, doses, penetration depths (R_p) and range distributions (ΔR_p) for B implantations into Nb_3Al substrates.

Energy KeV	Doses $\frac{ions}{cm^2}$ (10^{16})	R_p microns	ΔR_p microns
1000	10.8	1.600	0.320
600	10.0	1.180	0.295
400	17.1	0.850	0.253
320	14.0	0.720	0.230
160	29.4	0.400	0.164
80	18.7	0.180	0.103
30	9.7	0.070	0.053

Table III

Electron Beam Annealing Conditions

	C implanted samples	B implanted samples
Power density, KW/cm^2	25	5
Diameter of beam, mm	2	2
Voltage, KV	30	16
Current, mA	10	10
Pulse duration, msec	5	5
Pulse frequence, sec	1	5
Number of pulses	1 and 3	20

Table IV

Absorption of Cr radiation by $Nb_3Al_{0.5}B_{0.5}$

Angle of Incidence of X-rays degrees	Penetration depth for 90% absorption of X-rays microns
40	2.4
30	1.9
20	1.3
10	0.65
5	0.33

Table V

Comparison of theoretical and experimental dopant profiles for a B implanted sample annealed at 850°C for 24 hours.

Depth into sample microns	Theory			Experiment			
	$B^{(a)}$ At%	$Al^{(b)}$ At%	$\frac{B(At\%)}{Al(At\%)}$	$B^{(c)}$ API*	$Al^{(c)}$ API*	$\frac{B(API)^*}{Al(API)^*}$	$\frac{B(At\%)}{Al(At\%)}^{(d)}$
0.1	22.6	6.2	3.6	35	11	3.2	3.2
0.2	15.0	10.8	1.4	32	15	2.1	1.7
0.3	11.2	15.2	0.74	22	18	1.6	1.2
0.4	6.2	19.0	0.33	9	20	0.45	0.30
0.5	3.6	21.8	0.16	4	21	0.19	0.17
0.6	1.6	23.5	0.068	2	21	0.095	0.056

*Auger Peak Intensity

(a) from figure 2

(b) from figure 1

(c) from figure 5

(d) conversion of Auger peak intensities to At% from standards of known composition.

Table VI

Comparison of theoretical and experimental dopant profiles for a C implanted sample annealed at 805°C for 24 hours

Depth into sample microns	Theory			Experiment			
	$C^{(a)}$ At%	$Al^{(b)}$ At%	$\frac{C(At\%)}{Al(At\%)}$	$C^{(c)}$ API*	$Al^{(c)}$ API*	$\frac{C(API)^*}{Al(API)^*}$	$\frac{C(At\%)}{Al(At\%)}^{(d)}$
0.1	21.2	6.2	3.4	17.5	1.5	11.7	5.8
0.2	14.8	10.8	1.4	16	3.5	4.6	1.8
0.3	9.6	15.2	0.63	12	4.5	2.7	1.2
0.4	5.2	19.0	0.27	3	5.5	0.55	0.32
0.5	3.1	21.8	0.14	0	5.8	0.0	0.0
0.6	1.4	23.5	0.06	0	6.0	0.0	0.0

*Auger Peak Intensity

(a) from figure 3

(b) from figure 1

(c) from figure 6

(d) conversion of Auger peak intensities to At% from standards of known composition

Table VII

X-Ray Diffractometer Analysis of High Energy B Implantations into A-15 Nb_3Al

	Phases Observed	Change in lattice parameter of A-15 phase
-After Al diffusion anneal	-all of the A-15 peaks -several Nb peaks	
-After B implantations	-all of the A-15 peaks -several Nb peaks	increased by 2%
-After annealing up to 900°C	-all of the A-15 peaks -several Nb peaks	no further change
-After annealing at 950°C	-all of the A-15 peaks -several Nb peaks -several low intensity Nb_3B_2 peaks	no further change
-After annealing at 1050°C	-all of the A-15 peaks -decrease in intensity of the Nb peaks -increase in intensity of Nb_3B_2 peaks by a factor of 2	no further change

Table VIII

Change in Lattice Parameter of the Implanted Layers as a function of Ion Species, Energy, Dose and Heat Treatment

		Increase in Lattice Parameter
Low Energy C Implants (3.6×10^{17} ions/cm^2)	-After Furnace Annealing	.5%
	-After Electron Beam Annealing	1.5%
Low Energy B Implants (3.7×10^{17} ions/cm^2)	-After Furnace Annealing	1 %
	-After Electron Beam Annealing	2 %
High Energy B Implants (11.0×10^{17} ions/cm^2)	-After Furnace Annealing	2 %

Appendix B

MELT SPINNING AND PHASE TRANSFORMATIONS OF $V_2CrAl_{1-x}B_x$ AND $Ti_3Nb_6Mo_3Si_4$ ALLOYS

BRIAN SCOTT SMITH, RANDOLPH ARTHUR SMITH AND MIREILLE TREUIL CLAPP
Department of Mechanical Engineering,
University of Massachusetts,
Amherst, MA 01003

ABSTRACT

Melt Spinning was used to rapidly quench $V_2CrAl_{1-x}B_x$ and $Ti_3Nb_6Mo_3Si_4$ alloys. Melt spinning had very little effect on the crystal structure of the $V_2CrAl_{1-x}B_x$ alloys. However, a new $(NbTiMo)_3Si$ A-15 phase was found by rapid quenching of the $Ti_3Nb_6Mo_3Si_4$ alloys; the lattice parameter was 5.08 Å. Melt spinning increased the Vickers microhardness values of the $V_2CrAl_{1-x}B_x$ alloys from 500 to 750, and of the $Ti_3Nb_6Mo_3Si_4$ alloys from 1000 to as high as 1675. Melt spinning increased the superconducting transition temperature of the $Ti_3Nb_6Mo_3Si_4$ alloys from 1.9 to 3.4K.

INTRODUCTION

A great deal of interest has been focused on the A-15 structure because of its advantageous superconducting properties such as high superconducting transition temperature T_c. Many of the high T_c A-15's are metastable and have been processed by such techniques as sputtering, chemical vapor deposition, ion implantation and rapid quenching. This particular work concerns the effect of chill block melt spinning (CBMS) on A-15 phase stability and superconducting transition temperature; CBMS is a very rapid quenching technique capable of achieving cooling rates of 10^6 K/sec. The particular alloys studied were $V_2CrAl_{1-x}B_x$ and $Ti_3Nb_6Mo_3Si_4$. These alloys were chosen for several reasons. Most research has concentrated on binaries and ternaries; much less has been done on quaternaries. The particular combination of atoms agreed well with Hartsough's rules for A-15 phase stability (1). The transition elements have a high probability of forming the A-15 phase. The atomic radius ratio of the transition elements to the non-transition elements is favorable. The electron to atom ratio is 4.75 which is optimum for A-15 phase formation as well as high T_c superconductors.

EXPERIMENTAL PROCEDURE

Samples were prepared from high purity powders, compacted under pressure and arc-melted under an ultra-pure argon atmosphere.

A schematic of the chill block melt spinning apparatus used in this research is shown in Figure 1. The master alloy was melted with a 2.5 kW induction heater under an argon pressure of about 500 torr. When the alloy became visibly molten, the induction current was shut off and, simultaneously, argon pressure was applied above the melt. As a result, a molten jet was ejected from the crucible nozzle onto the outer surface of the copper substrate wheel (178 mm diameter) which was rotating at several thousand rpm. The ejected melt was rapidly quenched on the wheel surface in the form of thin ribbons. For all melt spinning experiments, the melt jet was incident at an angle of 15^o to the perpendicular to the wheel surface.

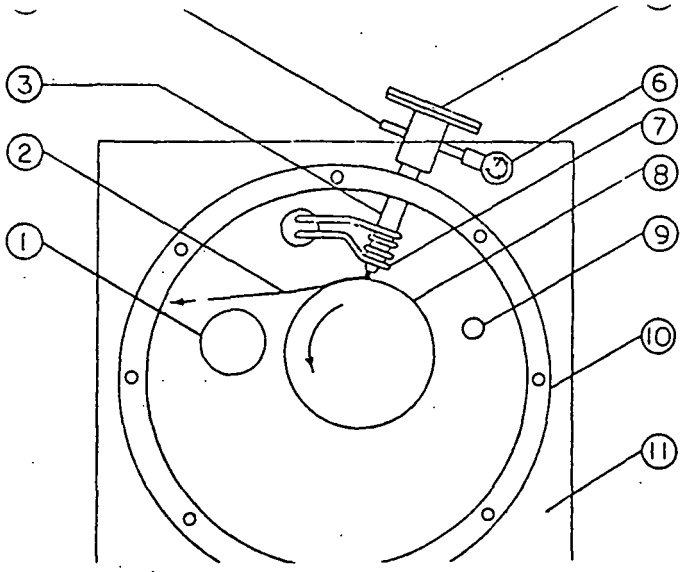

(1) Evacuation port; (2) Cast ribbon; (3) Crucible; (4) Argon gas inlet; (5) Viewport; (6) Vacuum gauge; (7) Induction coil; (8) Copper substrate wheel; (9) Argon gas inlet; (10) Steel chamber; (11) Lexan cover plate.

FIG. 1. Schematic of chill block melt spinning machine - front view.

As depicted in Figure 2(a), a 15 mm o.d. clear-fused quartz crucible was used for melt spinnning the $V_2CrAl_{1-x}B_x$ alloys. The nozzle orifice was comprised of a 3 mm length of precision (1.0 mm i.d.) quartz capillary joined to the end of the quartz crucible. To achieve temperatures high enough to induction melt these alloys, a 0.025 mm niobium foil radiation shield was inserted into the base of the crucible; this thin shield radiated heat back to the specimen and raised the temperature of the specimen above its melting point. The above crucible design was not adequate for processing the $Ti_3Nb_6Mo_3Si_4$ alloy, primarily because this alloy has a melting point much higher than that of clear-fused quartz. This problem was solved by suspending the sample in such a way that it did not touch the crucible. This eliminated heat conduction from the sample to the crucible. This also prevented any contamination to the sample from the crucible. The special apparatus designed for suspending the sample is shown in Figure 2(b). The sample was arc melted around the end of a section of molybdenum wire (5 cm long, 1 mm o.d.); Mo was selected because of its high melting point and its presence in the sample. A quartz crucible 4.5 cm long with a 1.5 mm nozzle i.d. was positioned vertically above the copper wheel. The sample was suspended 5 mm above the crucible nozzle. A 12.5 cm i.d. 6 turn induction coil was used for heating. The instant the sample melted and began to fall, the ejection pressure was applied.

Identification of the phases present in the arc-melted and melt-spun specimens was made by x-ray diffraction analysis using Cu radiation. The hardness of specimens was measured by a Vickers microhardness tester with a 50 g load. Superconducting transition temperature was monitored by a conventional four point probe resistive technique.

RESULTS

Table 1 shows the experimental results and corresponding process parameters of chill block melt spinning $V_2CrAl_{1-x}B_x$ and $Ti_3Nb_6Mo_3Si_4$ alloys. The V_2CrAl and $V_2CrAl_{0.75}B_{0.25}$ compositions were cast into ductile, continuous ribbons 230-250 mm in length. In contrast, the cast products of the $V_2CrAl_{0.5}B_{0.5}$ and $Ti_3Nb_6Mo_3Si_4$ compositions were in the form of brittle ribbon fragments with maximum lengths of 13 mm.

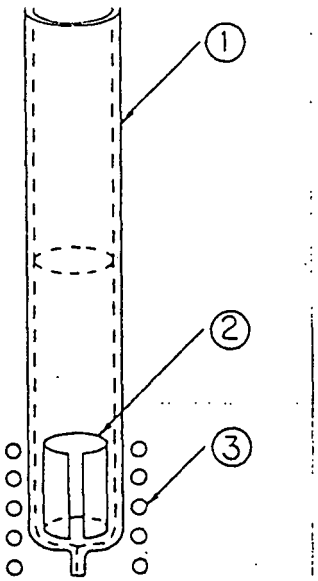

(1) 19 mm o.d. clear-fused-quartz crucible; (2) Nb foil (0.025 x 40 mm) radiation shield; (3) 1/8" 5 turn copper induction coil.

FIG. 2(a) Quartz crucible with niobium foil radiation shield.

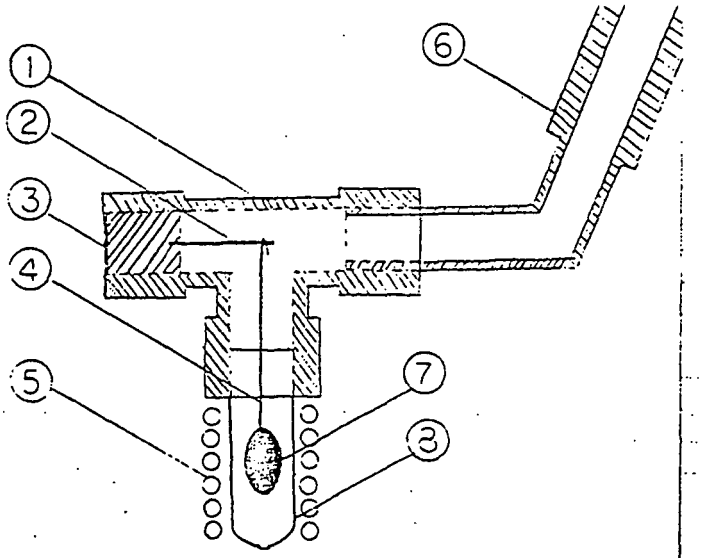

(1) Ultra-torr cajon tee; (2) Cu support wire; (3) rubber stopper; (4) Molybdenum wire; (5) 1/8" 6 turn induction coil; (6) Ejection pressure inlet; (7) Sample; (8) Quartz crucible.

FIG. 2(b) Vertical suspension apparatus.

TABLE 1. $V_2CrAl_{1-x}B_x$ and $Ti_3Nb_6Mo_3Si_4$ chill block melt spinning data

Sample Composition	Nozzle Diameter (mm)	Nozzle-Wheel-Gas (mm)	Ejection Pressure (psig)	Substrate Surface Speed (m/sec)	Ave. Ribbon Thickness (μm)	Ave. Ribbon Width (mm)
V_2CrAl	1.0	3.0	8	37	38	2.2
$V_2CrAl_{0.75}B_{0.25}$	1.0	3.0	8	37	29	1.9
$V_2CrAl_{0.5}B_{0.5}$	1.0	3.0	8	37	32	2.1
$Ti_3Nb_6Mo_3Si_4$ (#1)	1.5	2.0	8	28	97	2.0
$Ti_3Nb_6Mo_3Si_4$ (#2)	1.5	2.0	8	37	120	1.8

$V_2CrAl_{1-x}B_x$: Vickers micro-hardnesses of arc-melted and melt-spun specimens are given in Table 2. The H_v of arc-melted specimens increased with increasing boron content; i.e., the H_v of arc-melted $V_2CrAl_{0.5}B_{0.5}$ was about 20% higher than that of arc-melted V_2CrAl. Furthermore, melt spinning markedly increased the H_v of a given composition. For example, melt spinning increased the H_v of V_2CrAl by about 50%. This behavior may be attributed to the characteristic fine grain sizes produced by rapid quenching.

The results of the structural analyses of the $V_2CrAl_{1-x}B_x$ alloys are shown in Table 3. A single-phase, VCr bcc solid solution formed in arc-melted V_2CrAl. Alloying with boron resulted in the formation of second and third phases - tetragonal V_3B_2 and Cr_5B_3. Melt spinning decreased the amounts of V_3B_2 and Cr_5B_3 phases formed in the $V_2CrAl_{0.5}B_{0.5}$ and

TABLE 2. Vickers micro-hardness of arc-melted and melt-spun $V_2CrAl_{1-x}B_x$

Sample Composition	H_V (kg/mm^2) Arc-Melted	Melt-Spun
V_2CrAl	480	700
$V_2CrAl_{0.75}B_{0.25}$	550	790
$V_2CrAl_{0.5}B_{0.5}$	570	740

TABLE 3. Phases present in arc-melted and melt-spun $V_2CrAl_{1-x}B_x$

	Arc-Melted		Melt-Spun	
Compositions	Phases Present	Intensity (*)	Phases Present	Intensity (*)
V_2CrAl	VCr bcc	(100)	VCr bcc	(100)
$V_2CrAl_{0.75}B_{0.25}$	VCr bcc	(100)	VCr bcc	(100)
	V_3B_2 tetragonal	(8)	V_3B_2 tetragonal	(8)
$V_2CrAl_{0.5}B_{0.5}$	VCr	(100)	VCr bcc	(100)
	V_3B_2 tetragonal	(27)	V_3B_2 tetragonal	(10)
	Cr_5B_3 tetragonal	(19)	Cr_5B_3 tetragonal	(3)

*Denotes relative intensity of the most prominent peak of the phase.

$V_3CrAl_{0.75}B_{0.25}$ compositions. The V_2CrAl composition was not affected by melt spinning.

There was no indication of an onset of superconducting transition in the $V_2CrAl_{1-x}B_x$ alloys in either the arc-melted samples above 4.5 K or in the melt-spun samples above 1.6 K.

$Ti_3Nb_6Mo_3Si_4$: The Vickers microhardness results are given in Table 4. The values of hardness are very high, especially for the melt-spun samples.

The results of the crystal structure analysis for the $Ti_3Nb_6Mo_3Si_4$ alloys are given in Table 5. A Nb-Ti-Mo bcc solid solution and a high temperature $(NbTiMo)_5Si_3$ tetragonal phase were observed in all three samples. In addition, a new $(NbTiMo)_3Si$ A-15 phase was discovered in the more rapidly quenched sample (37 m/s).

TABLE 4. Micro-hardness results for $Ti_3Nb_6Mo_3Si_4$

Sample	Vickers Hardness (kg/mm^2)
Arc-Melted Button	1030
Melt-Spun Sample #1 (28 m/s)	1675
Melt-Spun Sample #2 (37 m/s)	1300

TABLE 5. Structural analysis of $Ti_3Nb_6Mo_3Si_4$

Sample	Phases Identified	Intensities (*)
Arc-Melted Button	Nb-Ti-Mo bcc solid solution	100
	High temperature $(NbTiMo)_5Si_3$, tetragonal	52
Melt-Spun Sample #1 (28 m/s)	Nb-Ti-Mo bcc solid solution	100
	High temperature $(NbTiMo)_5Si_3$, tetragonal	41
Melt-Spun Sample #2 (37 m/s)	Nb-Ti-Mo bcc solid solution	100
	High temperature $(NbTiMo)_5Si_3$, tetragonal	52
	$(NbTiMo)_3Si$, A-15	50

*Denotes relative intensity of the most prominent peak of the phase.

The interplanar spacings (d) of the bcc phases were 2.7% smaller than those of pure Nb. This was attributed to the presence of the smaller Mo atom. Similarly, the d values of the tetragonal phase were 1% smaller than those of the high temperature Nb_5Si_3 phase. As the quenching rate increased, the amount of the tetragonal phase decreased.

Eleven A-15 planes were conclusively identified. The lattice parameters calculated from the individual hkl reflections of the A-15 phase were used to determine a_o, as can be seen in Figure 3, and was found to be 5.08 Å.

The results of the superconducting transition temperature measurements are summarized in Table 6. All of the alloys were found to be superconducting. Melt spinning increased the T_c onset from 1.9 to 3.4 K. The two melt-spun samples were similar; the presence of the A-15 phase did not significantly affect T_c.

CONCLUSIONS

The Vickers hardness of 1675 for the $Ti_3Nb_6Mo_3Si_4$ melt spun samples is unusually high. This can be compared to 1100 for the hardest marten-

TABLE 6. Superconducting transition temperatures for $Ti_3Nb_6Mo_3Si_4$

Sample	T_c onset °K	T_c mid point °K
Arc-Melted	1.9	1.8
Melt-Spun Sample #1 (28 m/s)	3.4	2.9
Melt-Spun Sample #2 (37 m/s)	3.4	2.3

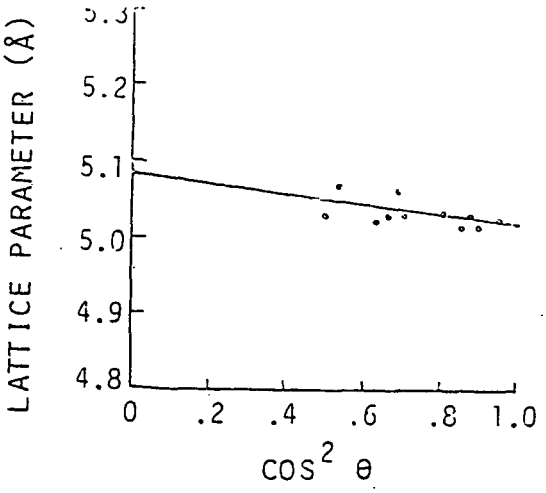

FIG. 3. Lattice parameter of the A-15 phase.

sitic steels and to 2000 for silicon carbide. Furthermore, slight modifications in composition can significantly affect hardness. It is, therefore, planned to continue work on the hardness of this particular alloy system and to further investigate the use of melt spinning to search for new extremely hard materials.

Melt spinning had very little effect on the structure of the $V_2CrAl_{1-x}B_x$ alloys. However, the effect was far more pronounced on the $Ti_3Nb_6Mo_3Si_4$ alloys. A new $(NbTiMo)_3Si$ A-15 phase was found as a result of the more rapid quenching. Liquid quenching has been effective in producing other A-15 phases such as Nb_3Si and Nb_3Ge [2]. The lattice parameter of the new $(NbTiMo)_3Si$ A-15 phase was 5.08Å. This is intermediary between values of 5.12Å for Nb_3Si and 4.89Å for Mo_3Si.

Melt spinning increased the T_c of the $Ti_3Nb_6Mo_3Si_4$ alloys from 1.9 K to 3.4 K. Solid solutions of Nb-Ti and Mo-Nb have T_c's that range from below 1K to above 9K [3]. A-15 Mo_3Si has a T_c of 1.3K [4], and water quenched $Ti_{54}Nb_{12}Mo_{34}$ a T_c of 3.3K [5]. The presence of the A-15 phase did not appear to affect the superconductivity of the alloy. The T_c of A-15's can be drastically lowered by poor stoichiometry and significant disorder.

Work is continuing on these alloys. The quenching rate is being increased by increasing the wheel speed, decreasing the ejection pressure and decreasing the nozzle diameter. The amount and stoichiometry of the A-15 phase should improve. Annealing should improve its ordering. Any effect on T_c will be noted.

REFERENCES

1. Hartsough, L.D., J. Phys. Chem. Solids 35, 1691 (1974).
2. Waterstrat, R.M., F. Haenssler, J. Muller, J. Appl. Phys. 50 (7), 4763 (1979).
3. Hardy, G.F., J.K. Hulm, Phys. Rev. 87, 884 (1953); 93, 1004 (1954).
4. Hulm, J.K., R.D. Blaugher, Phys. Rev. 123, 1569 (1961).
5. Cotton, W.L., R. Taggert, D.H. Polonis, Script. Metal. 8, 329 (1974).

This research was sponsored by the Department of Energy under Contract No. DE-AC02-80ER10666.A004.